Technical Report

TR-07-09

Geochemical investigation of iron transport into bentonite as steel corrodes

Fiona Hunter, Fiona Bate, Tim Heath, Andrew Hoch
Serco Assurance

September 2007

Svensk Kärnbränslehantering AB
Swedish Nuclear Fuel
and Waste Management Co
Box 5864
SE-102 40 Stockholm Sweden
Tel 08-459 84 00
+46 8 459 84 00
Fax 08-661 57 19
+46 8 661 57 19

Geochemical investigation of iron transport into bentonite as steel corrodes

Fiona Hunter, Fiona Bate, Tim Heath, Andrew Hoch
Serco Assurance

September 2007

Executive summary

In Sweden and Finland, it is proposed that spent nuclear fuel will be encapsulated in sealed cylindrical canisters, for disposal in a geologic repository, either in vertical boreholes (KBS-3V) or in long horizontal boreholes (KBS-3H). The canisters will consist of a thick cast iron insert and a copper outer container, and each canister will be surrounded by a compacted bentonite clay buffer. Both the canister and the surrounding bentonite act as engineered barriers to prevent release of radionuclides into the biosphere. For example, bentonite swells up in the presence of water reducing the likelihood of the formation of cracks in the clay, and therefore hindering the flow of groundwater. Equally, the non-corroding properties of copper maintain an intact, physical barrier to radionuclide release.

However, it is important to investigate the possible consequences if a failure of these physical barriers was to occur. For instance, if mechanical failure of the copper outer container were to occur then groundwater could enter the annulus and reach the cast iron insert. This would result in anaerobically corroded iron from the cast iron insert interacting with the bentonite surrounding the canisters. Reducing (anaerobic) groundwater conditions are expected once the repository is sealed and any remaining oxygen has been used up. The presence of anaerobically corroded iron in groundwater raises the question of how the bentonite will be affected by this process. In particular, will the important swelling properties of the bentonite be lessened, which may lead to a less effective physical barrier to radionuclide release?

In the case of the KBS-3H concept, mechanical failure of the copper outer container could lead to interaction between anaerobically corroded iron and bentonite, as above. However, direct contact between anaerobically corroding carbon steel and bentonite is also likely because of the presence of perforated carbon steel support structures in the long horizontal boreholes. Therefore it is also important to consider the effect of anaerobically corroding carbon steel on the bentonite physical barrier.

Work Package 2.3 of the European collaborative project Near Field PROcesses (NF-PRO, F16W-CT-2003-02389) has been charged with ‘investigating the interactions between corrosion products from iron and copper canisters with the bentonite and the effects on the engineered barrier system’. As part of the NF-PRO project, an extensive experimental programme has been carried out over several years to study the interactions between anaerobically corroding carbon steel or cast iron and bentonite. Drawing on the results of the experimental programme, a modelling investigation has been carried out to help bring together a more complete picture of the interactions between the corroding iron and bentonite. The purpose of this report is to describe the modelling work that has been carried out, and the conclusions that have been reached.

The experimental programme has carried out a series of long term experiments looking at anaerobic corrosion of carbon steel or cast iron in compacted MX-80 bentonite at 30°C or 50°C. A wide range of analytical characterisation was carried out and showed that the iron produced by corrosion has penetrated into the bentonite matrix. In the bentonite the concentration of iron decreased with increasing distance away from the iron-bentonite interface, with local iron concentrations as high as 20 wt % in some experiments.

Using the experimental data as a guide, a modelling investigation has been carried out. The objectives of the modelling investigation were:

- To develop a geochemical model of the transport of iron into bentonite based on the clear experimental evidence of the penetration of iron into bentonite.
- To improve our understanding of the desaturation of the bentonite as water is consumed during the corrosion process and the resultant gas(es) escapes.

The production of iron from the corroding source was modelled using a rate of gas evolution that had been fitted. A mass balance was carried out to compare the predicted amount of iron produced as a result of the evolved gas measurements (4.5 wt % of iron), with the bulk bentonite analysis (6.6 wt % of iron) and showed that the predicted amount of iron was slightly lower, but reasonable considering the experimental uncertainty in the measured gas volumes, and the analytical uncertainty of iron concentration measurement within the bentonite.

It was shown that ion exchange and surface complexation processes do not provide sufficient sorption to predict the high amount of iron observed in the solid phase. Therefore alternative processes, such as iron-containing mineral formation or mineral transformations, were also suggested to account for the amount of iron observed within the bentonite phase. Magnetite was identified as the most thermodynamically stable solubility-limiting phase under the experimental conditions. Formation of pyrite was excluded due to kinetic barriers that would hinder its formation under the experimental conditions and timescale.

A one-dimensional transport model was constructed to include all relevant processes. The simulations considered the diffusive transport of Fe^{2+} ions away from a corroding source, using the rate of gas evolution resulting from the corrosion process. Ion exchange and surface complexation processes were allowed within the bentonite which would provide sorption of iron onto and within the bentonite solid. The pH was buffered by allowing protonation and deprotonation of the surface sites of the bentonite solid. In addition, saturation of iron-containing minerals was permitted.

The base case model suggests that about 4.4 wt % of iron could form in the bentonite if the formation of magnetite was allowed. However, the maximum theoretical amount of iron available from the source term is limited to 4.5 wt % of iron by the cumulative gas evolution rate, which is lower than the observed amount of iron in the bulk bentonite (6.6 wt %). A variant case, with a saturated solution of $Fe(OH)_{2(s)}$ as the source term was carried out and predicted that much greater amounts of magnetite could form within the solid phase, with a maximum of 58 wt % of iron. The variant case is considered to be an extreme scenario, consistent with a higher aqueous concentration of iron in the source cell that is much greater than that predicted by fitting of the measured gas evolution rate data. The amount of iron predicted within the solid phase in the base case and the variant case are considered to be bounding scenarios that encompass the experimental results.

Overall, the one-dimensional geochemical model of iron transport away from a corroding steel surface into bentonite required the formation of iron-containing minerals to predict the amounts of iron observed within the solid phase. This may take place by supersaturation of iron-containing mineral phases which could lead to the formation of solid phases such as magnetite, or mineral transformations (not modelled in this study).

It is important to understand how the environment close to the iron is affected as corrosion processes consume water and produce hydrogen gas. As water is consumed it is possible that desaturation of the bentonite may take place, which then would provide a pathway for the escape of gas away from the corrosion site. Alternatively, if desaturation does not occur, then conventional ideas suggest that significant build up of gas (several MPa pressure) would be required for the gas to force its way through the bentonite. Scoping calculations of gas migration through a cylindrical bentonite sample (like those used in the corrosion experiments) suggest the gas pressure would peak at around 2 MPa, which is less than the apparent gas entry pressure of the bentonite, before decreasing towards a steady state with a maximum overpressure of about 1 MPa. The gas saturation would increase to about 1%, which is sufficient for the gas to escape from the bentonite.

Contents

1 Introduction

In Sweden and Finland, it is proposed that spent nuclear fuel will be encapsulated in sealed cylindrical canisters, for disposal in a geologic repository, either in vertical boreholes (KBS-3V) or in long horizontal boreholes (KBS-3H) /1/. The canisters will consist of a thick cast iron insert and a copper outer container, and each canister will be surrounded by a compacted bentonite clay buffer. Both the canister and the surrounding bentonite act as engineered barriers to prevent release of radionuclides into the biosphere. For example, bentonite swells up in the presence of water reducing the likelihood of the formation of cracks in the clay, and therefore hindering the flow of groundwater. Equally, the non-corroding properties of copper maintain an intact, physical barrier to radionuclide release.

However, it is important to investigate the possible consequences if a failure of these physical barriers was to occur. For instance, if mechanical failure of the copper outer container were to occur then groundwater could enter the annulus and reach the cast iron insert. This would result in anaerobically corroded iron from the cast iron insert interacting with the bentonite surrounding the canisters. Reducing (anaerobic) groundwater conditions are expected once the repository is sealed and any remaining oxygen has been used up. The presence of anaerobically corroded iron in groundwater raises the question of how the bentonite will be affected by this process. In particular, will the important swelling properties of the bentonite be lessened, which may lead to a less effective physical barrier to radionuclide release?

In the case of the KBS-3H concept, mechanical failure of the copper outer container could lead to interaction between anaerobically corroded iron and bentonite, as above. However, direct contact between anaerobically corroding carbon steel and bentonite is also likely because of the presence of perforated carbon steel support structures in the long horizontal boreholes. Therefore it is also important to consider the effect of anaerobically corroding carbon steel on the bentonite physical barrier.

Work Package 2.3 of the European collaborative project Near Field PROcesses (NF-PRO, F16W-CT-2003-02389) has been charged with ‘investigating the interactions between corrosion products from iron and copper canisters with the bentonite and the effects on the engineered barrier system’. As part of the NF-PRO project, an extensive experimental programme has been carried out over several years to study the interactions between anaerobically corroding carbon steel or cast iron and bentonite /2/. Drawing on the results of the experimental programme, a modelling investigation has been carried out to help bring together a more complete picture of the interactions between the corroding iron and bentonite. The purpose of this report is to describe the modelling work that has been carried out, and the conclusions that have been reached.

1.1 Summary of results from the experimental programme

The experimental programme carried out long term experiments looking at anaerobic corrosion of carbon steel and cast iron in bentonite. Full details of the experimental programme and subsequent analyses are reported in Smart et al. 2006 /2/. The subsequent modelling investigation that is the purpose of this report focussed on particular aspects of their work and it is useful to summarise pertinent results from the analytical data before describing the modelling objectives.

The laboratory programme carried out a series of long term experiments (~ 833 days) looking at anaerobic corrosion of carbon steel or cast iron in compacted Volclay MX-80 bentonite. Each experiment was placed in contact with a simple artificial groundwater at 30°C or 50°C. For the carbon steel experiments, 5mm lengths of steel wire were mixed with dry MX-80 bentonite and

compacted into a cylindrical piece of bentonite. Then these were loaded into a stainless steel sample holder which was designed to allow the artificial groundwater to enter and gas to escape through porous sintered metal filters. Similar experiments were set up containing a steel coupon and a cast iron coupon. The samples were prepared in air and then evacuated and placed in an inert gas glovebox before the experiments were saturated with groundwater and evolved gas was collected.

The very small volume of porewater within compacted bentonite makes analysis of the in situ porewater near impossible without squeezing, which is likely to affect the chemistry of the resultant water, Therefore, an additional experiment was set up using an uncompacted bentonite (slurry) mixed with carbon steel wires, which allowed the pH and elemental chemistry to be measured.

A wide range of analytical characterisation was carried out. The samples were analysed using X-ray powder diffraction under both anoxic and oxic conditions (XRD), Fourier transform infrared spectroscopy (FTIR), laser Raman spectroscopy, scanning electron microscopy (SEM) with energy dispersive X-ray analysis (EDS) and electron microprobe analysis (EPMA), transmission electron microscopy (TEM) with EDS and electron diffraction, and Mössbauer spectroscopy. In addition, exchangeable cation content, cation exchange capacity (CEC), total chemical composition, swelling pressure and hydraulic conductivity of the bentonite samples were measured.

The relevant key conclusions of the experimental study showed that:

- The iron penetrated the MX-80 bentonite, giving local iron concentrations as high as 20 wt % (EPMA analysis). The total iron content was much higher in bentonite from tests with many corroding carbon steel wires than in fresh MX-80, or MX-80 in contact with a single coupon of ferrous material. The iron content decreased with increasing distance from the corroding surface.
- The predominant corrosion product that formed on the anaerobically corroded steel wires was identified as magnetite, and formed a thin layer (lasar Raman spectroscopy). On the cast iron and carbon steel coupons, the corrosion products were magnetite, hematite and goethite. No $Fe(OH)_2$ was identified as a corrosion product.
- In the presence of corroding steel wires, Fe^{2+} was the dominant anaerobic corrosion product (Mössbauer spectroscopy).
- There was no evidence for the presence of any separate iron oxide or oxyhydroxide phases in the bentonite matrix (XRD, FTIR, TEM).
- There was no indication that iron produced by the low temperature anaerobic corrosion of steel in bentonite caused a transformation of montmorillonite to a different iron-rich mineral phase such as chlorite or berthierine (XRD).

Clear evidence for the penetration of iron into the bentonite after the corrosion had taken place is given in Figure 1-1. This shows an EMPA image of the locally high distribution of iron within compacted bentonite after the carbon steel wire corrosion experiment at 30°C. The EMPA map for corroding steel wire at 30°C (after removal of background iron) reveals that the highest iron concentrations were observed within 100 μm distance from the corroding wire surface, with a maximum recorded value of about 7.5 wt % at 75 μm (Figure 1-2).

1.2 Objectives of the modelling investigation

Using the experimental data as a guide, a modelling investigation has been carried out. The objectives of the modelling investigation were:

- To develop a geochemical model of the transport of iron into bentonite based on the clear experimental evidence of the penetration of iron into bentonite.

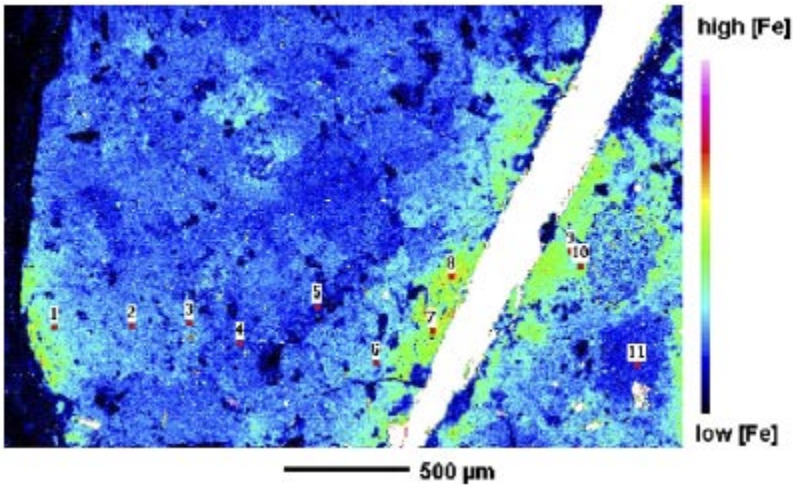

Figure 1-1. *Distribution of iron in compacted bentonite kept in contact with a carbon steel wire (central white area) for 829 days at 30°C. This image was generated by electron microprobe analysis.*

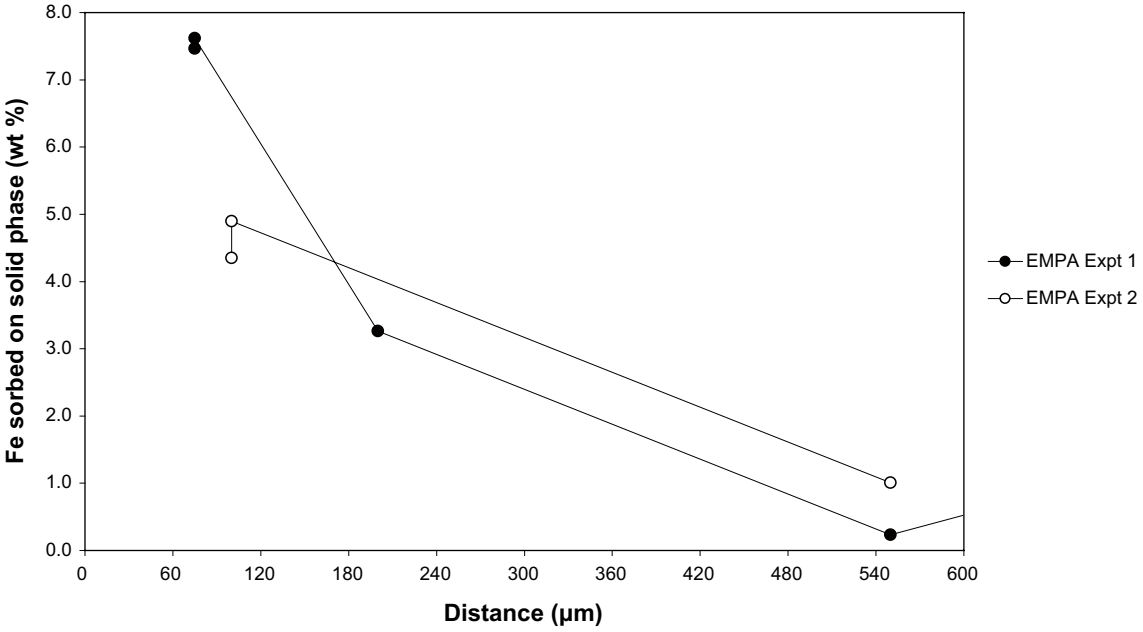

Figure 1-2. *Distribution of iron in compacted bentonite plotted against distance from the carbon steel wire, as mapped in Figure 1-1. The background iron (2.4 wt %) has been removed from each observation.*

- To improve our understanding of the desaturation of the bentonite as water is consumed during the corrosion process and the resultant gas(es) escapes.

Preliminary calculations have been carried out to investigate processes involving transport of iron into bentonite /2/. These preliminary calculations show that a simple model for the sorption of iron onto the solid phase cannot explain the iron profile within the bentonite unless arguments are invoked to increase both the tortuosity and retardation factor of the bentonite by one order of magnitude (effectively slowing the rate of diffusion by two orders of magnitude). Therefore, a more in-depth investigation is considered as part of the current geochemical transport modelling objective.

Where possible the experimental results have been used as modelling input data, or the use of published literature if this has not been possible. Modelling of these processes builds confidence in our understanding of the chemical processes that are taking place. Such understanding is important in applying the experimental results obtained under laboratory conditions and over laboratory timescales, to those applicable to the repository and assessment timescales.

The first modelling objective to develop a geochemical transport model of the interactions of iron with compacted bentonite required several building blocks. Firstly, a model of bentonite porewater chemistry was required. Secondly, an understanding of the rate of production of iron from the corroding source was required. Thirdly, the thermodynamic formation of iron containing minerals was considered. Fourthly, a one dimensional transport model based on these building blocks was built up, and allowed iron to diffuse away from the corroding source and penetrate into the surrounding bentonite. The transport model prediction was then compared with the observations of the extent and amount of iron measured within bentonite. The corroding carbon steel wire experiment at 30°C was used for the comparison because this had the clearest evidence of iron penetration into the bentonite.

The reasoning for each of the required steps to construct a geochemical transport model is summarised below:

- Initially, an understanding of the porewater of compacted bentonite is needed. Since is it near impossible to measure an in situ compacted bentonite porewater composition, a chemical equilibrium model was required. Therefore, the selection and verification of a literature model of compacted bentonite porewater was carried out, followed by the application of this model to the MX-80 bentonite used in the experimental programme.
- Due to the structure of montmorillonite, the mineral that forms a major component of bentonite, exchange between cations that are present in the interlayers of the clay and the porewater is expected to take place. Similarly, sorption of cations from the porewater onto external clay surfaces is expected to occur. Therefore, the sorption processes of ion exchange and surface complexation were needed within the model. Usefully, the literature bentonite porewater model included ion exchange of the major porewater cations (sodium, potassium, magnesium and calcium) and surface complexation of protons. Hence, the model would only require extending to include sorption of iron by ion exchange and surface complexation.
- An estimation of the rate of production of iron from the corroding source is fundamental to setting up a transport model. Two approaches were used, based on (i) the measured gas evolution rate resulting from corrosion and the corresponding estimated amount of iron released into solution at any time and, (ii) a high end estimate based on the aqueous iron concentration that would be achieved with a saturated solution of iron mineral as the corroding source.
- It is important for several reasons to be able to predict the thermodynamic likelihood of the formation of iron-containing minerals under the experimental conditions. First, this information can be compared with the experimental evidence for iron-containing minerals. Second, in tandem with the experimental evidence, this information helps with the decision of which iron-containing minerals could be considered as the modelled source of the corroding iron. Third, this information provides a prediction of thermodynamically stable minerals that may form within the bentonite. Therefore iron solubility limiting minerals were investigated under varying redox conditions and pH.
- Bringing all the above information together, the one-dimensional transport model considered diffusion of iron away from the corroding source and into compacted bentonite. Simultaneously, chemical reactions (sorption and mineral formation) were considered. The model predictions were compared with the observations, focusing on the corroding carbon steel wire experimental in compacted bentonite at 30°C that provided the clearest evidence of iron penetration into bentonite.

The second modelling objective to improve our understanding of the desaturation of the bentonite required a model of gas migration through the bentonite. This considered the consumption of water and production of gas as the corrosion process takes place. As water is consumed it is possible that desaturation of the bentonite may take place, which then would provide a pathway for the escape of gas away from the corrosion site. Alternatively, if desaturation does not occur, then significant build up of gas would be required for the gas to force its way through the bentonite. The gas migration model was based on available measured experimental data for the corrosion rate and the hydraulic properties of the bentonite, and scoping calculations were carried out to investigate whether desaturation is likely to occur.

Sections 2 to 4 detail the bentonite porewater modelling, the corroding iron source, and the solubility and sorption of iron, all of which are building blocks for the subsequent geochemical transport model (section 6). Section 5 details the gas migration modelling.

The geochemical modelling has been carried out using PHREEQC 12.2 /3/. The HATCHES NEA 17 database of thermodynamic constants, a well recognised, quality-assured database /4/, has been used to provide the underlying chemical data. The gas migration modelling was carried out using TOUGH2 /25, 26/.

2 Chemical equilibrium modelling of bentonite porewater

In order to provide a clear understanding of the processes involved, it is important to be able to predict the porewater chemistry of the bentonite used in the experimental programme before any iron corrosion products have been incorporated. However, the porewater in compacted bentonite is almost impossible to determine experimentally by chemical analysis; even at very high squeezing pressures it is difficult to obtain large enough quantities of pore water and it is unlikely that this sampled solution would be representative of the in situ compacted bentonite porewater. As a result, the properties of compacted bentonite porewater have been evaluated through circumstantial experimental evidence or physical-chemical modelling. Therefore, in this section, a model of porewater in equilibrium with the compacted bentonite that was used in the experimental programme was developed.

First, a literature model of compacted bentonite porewater was selected and its implementation in our calculations was verified. Then, the bentonite porewater model was tested against the analysed composition of a porewater in equilibrium with uncompacted bentonite (slurry) that was obtained from the experimental programme. Finally, the uncompacted bentonite porewater model was applied to the compacted MX-80 bentonite that had been used in the experimental programme.

Two model approaches have been used in recent evaluations of bentonite porewater chemistry. The traditional approach considers exclusively ion exchange at the siloxane surface (e.g. Wanner 1986 /5/) while more recent models include surface functional OH groups at the clay edge sites in addition to ion exchange (e.g. Wanner et al. 1994 /6/, Bradbury and Baeyens 1997 /7/, 2002 /8/, 2003 /9/). Both electrostatic surface complexation (e.g. Wanner et al. 1994 /6/, Ochs et al. 2004 /10/) and non-electrostatic surface complexation (Bradbury and Baeyens 1997 /7/, 2002 /8/, 2003 /9/) have been implemented within the alternative model approaches.

The approach used in this work was to take the compacted bentonite porewater equilibrium model developed by Bradbury and Baeyens 2002 /8/, 2003 /9/, hereinafter referred to as the 'Bradbury and Baeyens model'), and using this as a guide, to set up an equivalent chemical equilibrium model in PHREEQC 12.2. This allows comparison of this work against the Bradbury and Baeyens model as a verification test to check for consistency. The Bradbury and Baeyens model allows protonation and deprotonation of surface sites on the bentonite which will act to buffer the pH. Also, ion exchange between the major cations (Na^+, K^+, Mg^{2+}, Ca^{2+}) and the bentonite solid is permitted. Bradbury and Baeyens based their model on an MX-80 bentonite with similar composition to the MX-80 bentonite used in Smart et al. 2006 /2/. It was felt appropriate to develop our current MX-80 bentonite model by building on the work carried out by Bradbury and Baeyens, after the initial step of verification of the PHREEQC model against their published results. The verification of our PHREEQC model against Bradbury and Baeyens' work is detailed in Appendix 1.

2.1 Simulation of the bentonite porewater chemistry and comparison against observed data

The approach taken here has been to adapt the verified chemical thermodynamic model (Appendix 1) for the composition of bentonite used in the experimental programme, and check the adapted model against the experimental analysis of the bentonite porewater measured in a 30 wt % uncompacted bentonite slurry porewater that has no iron corrosion products.

The MX-80 bentonite used in the experiments by Smart et al. 2006 /2/ has a different composition to that modelled by Bradbury and Baeyens /8, 9/. Therefore the bentonite porewater model verified against Bradbury and Baeyens model was required to be adapted to the current experimental programme. The composition of the batch of MX-80 bentonite used in the experimental programme is reported in Table 2-1, and shows that this batch of bentonite has significantly more montmorillonite present (87% as opposed to 75% in the MX-80 modelled by Bradbury and Baeyens model), as well as a differing composition of accessory minerals (compare with Appendix 1).

The corrosion cell experiments were carried out using iron wires or carbon steel/cast iron coupons in compacted MX-80 bentonite with a dry density of 1,600 kg m^{-3} (Smart et al. 2006 /2/). The compacted bentonite cells were wetted with a simple artificial groundwater (31.56 g dm^{-3} NaCl and 1.06 g dm^{-3} Na_2CO_3, pH 10.4) but it is experimentally difficult to measure the equilibrated porewater composition due to the scarcity of available pore fluid. In order to get around this problem, a bentonite slurry was concurrently prepared, in air, in which the same simple artificial groundwater was equilibrated with the bentonite (30 wt % of solid) for several months and an analysis of the major element composition in the filtered, supernatant water was obtained (see first column of Table 2-3. The analysed porewater arising from the bentonite slurry was used to check the bentonite porewater model (detailed in the following sections).

2.1.1 Approach taken for modelling of uncompacted bentonite porewater

Initially, the approach taken was to predict the measured pH of 8.4 using the uncompacted bentonite (slurry) porewater model in equilibrium with appropriate minerals. Secondly, after it became clear that a good match to the pH was difficult, then the pH was fixed at the experimental value and more calculations were carried out. Each calculation was set up in two stages. First the surface complexation sites were equilibrated with a solution of pH 8.4 to give a set of surface sites conditioned to the specified pH. Then a second stage of the simulation took the conditioned surface and conducted an equilibrium calculation with the groundwater, minerals and exchangeable sites as required.

It is known that low quantities of NaCl are present within MX-80 bentonite. In addition, significant variability of the amount of NaCl is likely to be observed within individual batches of MX-80 bentonite due to the many-stage industrial process that purifies the raw material and includes washing and drying procedures that are likely to remove substantial amounts of

Table 2-1. Reported composition of MX-80 bentonite used in the experimental programme, Batch 2001-01, /11/.

Mineral	Composition (%)
Montmorillonite*	~ 87
Plagioclase feldspar	~ 4
Cristobalite	~ 3
Gypsum	~ 1
Muscovite	~ 1
Pyrite	< 1
Total**	~ 97

* The composition of the < 2 µm (clay) fraction, total CEC (Cu-exchange) and the extractable ions (ammonium exchange) was used to calculate the montmorillonite formula: $Na_{0.47}K_{0.01}Mg_{0.04}Ca_{0.09}(Si_{7.91}Al_{0.09})(Al_{3.11}Fe^{3+}_{0.37}Mg_{0.52})O_{20}(OH)_4$. ($Fe^{3+}$ has been assumed in the calculation of the formula, but this is not necessarily representative of the real situation.) Analysis of the bulk material by ICP-AES gives on average 2.8% Fe content.

** Note that 3% of the material has not been accounted for.

$NaCl_{(s)}$ /8/. It was noted that the sodium and chloride concentrations in the measured bentonite porewater slurry are higher than those in the artificial groundwater, and therefore the observed increases could only have come from the solid MX-80 phase. Since the increase in the concentration of these two elements was approximately equal, this was interpreted as being due to a small component of sodium chloride in the original solid or porewater and equivalent to an additional 0.095 mol dm^{-3} NaCl in the equilibrated slurry.

Since the measured ionic strength is about 0.7 mol dm^{-3}, the use of a method of ionic strength correction is needed to account for the formation of aqueous ion pairs. Initial calculations were carried out using the Davies ionic strength method /12/, but this method is not expected to be accurate at the measured ionic strengths of the bentonite slurry. Therefore, further calculations were performed using more appropriate ion activity treatments. Firstly, the specific ion interaction theory (SIT) approach (described in /13/) was applied using the HARPHRQ geochemical code version 2.0 /14/ and SIT interaction parameters from the NEA data reviews /e.g. 15/. Secondly, the Pitzer approach (e.g. /16/ and applied in /17/), was applied using PHREEQC and the Pitzer parameters and thermodynamic data provided with PHREEQC version 2.12 /3/.

2.1.2 Uncompacted bentonite (slurry) porewater model parameters

The bentonite slurry experiments were performed on a low density, uncompacted bentonite that gave a reasonable volume of the resulting bentonite porewater, sufficient enough to perform an elemental analysis and pH measurement. (A compacted bentonite would not provide enough porewater to allow easy analysis of the resultant bentonite porewater.)

The bentonite porewater model was set up using:

- 30 wt % bentonite slurry which equates to modelling 1 litre of porewater in contact with 0.435 kg bentonite.
- The minerals modelled were calcite, gypsum, cristobalite, celestite, pyrite and magnesium carbonate. The reasoning for this mineral selection is discussed below.
- The total cation exchange capacity (CEC) was taken to be 0.787 mol cation per kg of MX-80 bentonite /8, 9/. This value is comparable to CEC measurements taken during this experimental programme (0.885 mol kg^{-1} and 0.785 mol kg^{-1} for MX-80 extractions performed in air /2/). Therefore the use of the published CEC is assumed to be a reasonable approximation. (Indeed, a variant model calculation using a high CEC value of 1.6 mol kg^{-1} reported in this experimental programme for extractions under an inert atmosphere gave little change to the resultant simulated porewater composition.)
- The individual cation occupancies on ion exchange sites within MX-80 bentonite in equilibrium with air were taken from references /8/ and /9/. These parameters are shown in Appendix 1, Table A1.
- Assuming 87% of the bentonite is composed of montmorillonite, and a specific surface area of 31.3 $m^2\ g^{-1}$ (N_2 BET surface area /8, 9/), the total number of surface complexation sites in the experimental system was calculated, and used as an input parameter for the model.
- The bentonite was equilibrated with a simple groundwater ($NaCl/NaCO_3$, pH of 10.4, ionic strength of 0.57 mol dm^{-3}) to mimic the experimental procedure.
- The HATCHES NEA17 thermodynamic database was used for all calculations when simulating the experimental programme.
- The uncompacted bentonite (slurry) experiment was carried out under oxic conditions. (Note that the compacted bentonite experiments (and simulations) were carried out under anoxic conditions with an Eh of about –400 mV.)
- The presence of an additional 0.095 mol dm^{-3} NaCl was assumed in the equilibrated slurry (see section 2.1.1).

In order to model the complexity of the aqueous system, a mineral equilibrium was required for each new species analysed in the bentonite slurry porewater. The mineral equilibria were examined in detail. As the bentonite slurry mixture had been equilibrated for several months (not years), the slurry was deemed to be in equilibrium with those minerals that would come to equilibrium quickly (such as calcite, gypsum, and meta-stable minerals like cristobalite), but was thought unlikely to be in full equilibrium with 'unreactive' minerals that would typically take much longer to reach equilibrium at low temperatures (such as quartz, muscovite, plagioclase, montmorillonite). First the selection of minerals used by Bradbury and Baeyens for their bentonite porewater model (Appendix 1) was examined and calcite, celestite and gypsum were selected for further examination (fluorite, CaF_2, was disregarded since no measured concentrations for fluoride were available). Second, the characterisation of MX-80 mineralogy was examined (Table 2-1) and cristobalite and pyrite were added to the list of minerals under consideration.

The effect of each mineral equilibrium on pH was examined. For instance, calculations showed that inclusion of calcite within the model gave either (i) a low pH (7.7) at atmospheric pCO_2 levels, and caused precipitation of calcite (0.01 mol per litre of porewater) with a significant under-prediction of calcium or inorganic carbon concentration or both or, (ii) required significant amounts of dissolution of gypsum and precipitation of calcite at a fixed pH of 8.4 when calcite (and gypsum) were present, rendering the ionic strength unrealistically large (1.8 mol dm^{-3}). The other simulated minerals had comparably little effect on the pH. The inclusion of cristobalite gave a better match to aqueous silica concentrations than was the case for quartz.

At the measured pH of 8.4, the combination of observed calcium and inorganic carbon concentrations and equilibration with atmospheric carbon dioxide imply over-saturation with respect to calcite. Since the bentonite in this system is not compacted, the pH measurement was considered to be a reliable value for the bentonite porewater and the over-saturation of the analysed water with respect to calcite was considered either to be a real effect or to result from analytical uncertainty in the measured concentrations. Further calculations were therefore performed allowing some precipitation of calcite but leaving the solution a little oversaturated by fixing calcite saturation index (SI) with a value of 0.78. This value was selected as being typical of that for surface seawater, (since surface seawater is often oversaturated with respect to calcite) although it is acknowledged that this extent of over-saturation is less likely in the presence of the bentonite mineral surfaces. Examination of Table 2-1 shows that calcite has not been identified within this batch of MX-80, but it is noted that 3% of the bentonite material has not been accounted for.

Initial calculations showed a small discrepancy between the modelled sulphate concentration and the measured value, and therefore the amount of gypsum in equilibrium with the porewater was reduced slightly. From Table 2-1, it had been estimated that the 0.03 moles of gypsum were likely to be available in the MX-80 bentonite sample per litre of slurry porewater. However, this was a rough estimate and it was considered reasonable to lower the available gypsum to 0.02 mol dm^{-3} significantly improving the predicted sulphate agreement.

The final mineral assemblage used in the bentonite slurry model calculations included cristobalite, gypsum and celestite (to provide a match to strontium concentrations). The inventory of each mineral present within MX-80 (Table 2-1) has been set within the calculation to prevent the dissolution of a greater amount of mineral phase than is physically present, although the state of mineral equilibration was monitored to maintain mineral saturation (or oversaturation in the case of calcite). The inclusion of pyrite (FeS_2) in equilibration with the porewater simulates reducing conditions with a negative Eh and little effect on ionic strength. Pyrite has been identified within this batch of MX-80 bentonite, however significant additional amounts of pyrite are unlikely to precipitate unless microbially mediated sulphate reduction occurs and this is considered unlikely within the experimental environment.

2.1.3 Results of uncompacted bentonite (slurry) porewater model

The modelling results of the uncompacted bentonite (slurry) porewater composition and the effects of various ionic strength treatments are presented and compared with the analytical data from the experimental programme (Table 2-2 and Table 2-3). The model prediction is considered reasonable since all the modelled values fall within less than half an order of magnitude of the measured data.

Table 2-2. Model input parameter for uncompacted bentonite (slurry) porewater.

Description/ calculation name	Analysed bentonite slurry porewater	B-slurry_ Davies (PHREEQC)	B-slurry_ Davies (HARPHRQ)	B-slurry_ SIT (HARPHRQ)	B-slurry_ Pitzer (PHREEQC)
Simulation name		b-slurry_e17a	g17a	d17a	b-slurry_j17a
pH treatment		fixed	fixed	fixed	fixed
Ionic strength treatment		Davies	Davies	SIT*	Pitzer
Database used		HATCHES NEA17	HATCHES NEA17	HATCHES NEA17	PHREEQC Pitzer.dat
Mineral equlibrations†		Calcite (SI=0.78) Gypsum: (0.02 mol dm^{-3})	Calcite (SI=0.78) Gypsum: (0.02 mol dm^{-3})	Calcite (SI=0.78) Gypsum: (0.02 mol dm^{-3})	Calcite (SI=0.78) Gypsum: (0.02 mol dm^{-3}) Celestite
		Cristabolite Celestite $MgCO_3$	Cristabolite Celestite $MgCO_3$	Cristabolite Celestite $MgCO_3$	
Added NaCl (mol dm^{-3})		0.095	0.095	0.095	0.095
$Log_{10}(pCO_2)$ (atm)	in air	–3.5	–3.5	–3.5	–3.5
pH	8.4	8.4	8.4	8.4	8.4
Eh	oxidising	oxidising	oxidising	oxidising	oxidising
Ionic Strength (mol dm^{-3})	0.70	0.68	0.67	0.69	0.71

† $MgCO_3$ solid was predicted to become over-saturated and was allowed to precipitate in each case except the Pitzer calculation.

Table 2-3. Analysed uncompacted bentonite (slurry) porewater and comparison with refined model results.

Description/ calculation name	Porewater composition (mol dm^{-3})				
	Analysed bentonite slurry porewater	B-slurry_ Davies (PHREEQC)	B-slurry_ Davies (HARPHRQ)	B-slurry_ SIT (HARPHRQ)	B-slurry_ Pitzer (PHREEQC)
C_{inorg}	2.46E–03	2.1E–03	2.1E–03	2.0E–03	2.4E–03
Ca	9.98E–03	5.6E–03	5.6E–03	7.8E–03	7.3E–03
Cl	6.36E–01	6.4E–01	6.4E–01	6.4E–01	6.4E–01
K	3.07E–03	3.4E–03	3.2E–03	3.3E–03	3.4E–03
Mg	4.94E–03	3.4E–03	3.4E–03	4.4E–03	5.7E–03
Na	6.38E–01	6.6E–01	6.2E–01	6.2E–01	6.5E–01
SO_4^{2-}	1.56E–02	2.1E–02	2.0E–02	2.1E–02	2.1E–02
Si	3.20E–04	3.1E–04	3.1E–04	3.6E–04	–
Sr	2.51E–04	6.4E–04	4.7E–04	6.7E–04	5.3E–04

* Ion pair complexes inconsistent with the SIT approach were removed from the thermodynamic database.

Allowing restricted calcite formation (saturation index = 0.78) gives reasonable predictions of the concentrations of calcium and inorganic carbon. Restricting the amount of gypsum available for dissolution improves the agreement for sulphate but due to the gypsum/celesitite balance, this results in a strontium concentration greater than that observed experimentally. However, this is considered acceptable since strontium is a relatively minor component of the bentonite slurry water.

Comparison of the results using the various ion activity treatments shows that the predicted concentrations are similar in each case. The SIT and Pitzer approaches improve the agreement between the observed and modelled calcium concentrations slightly compared to the Davis appraoch. However, it was considered reasonable for subsequent calculations to use the Davies approach applied within PHREEQC because the uncertainty introduced by the Davies approach is expected to be small in comparison to other sources of uncertainty. Equally, it was more practical to use the Davies approach for subsequent calculations since this did not require (i) additional Pitzer coefficient for each ionic species, and (ii) the use of alternative geochemical modelling codes (HARPRRQ) that are more limited in scope for modelling several processes simultaneously.

In subsequent calculations, the uncompacted bentonite porewater model will be applied to the compacted MX-80 bentonite that had been used in the experimental programme. This is described below;

The compacted MX-80 bentonite used within the experimental programme has a dry density of 1,600 kg m^{-3}, hence the model of uncompacted bentonite slurry porewater required adaptation. The solid to liquid ratio of the uncompacted bentonite model was altered to suit compacted bentonite of appropriate dry density. The compacted bentonite required a liquid to solid ratio of 0.0125 dm^3 kg^{-1} corresponding to a model with one litre of porewater and 80 kg of MX-80. Additionally, the compacted bentonite model assumed low pCO_2 conditions with an Eh of –400 mV to simulate the anoxic, reducing conditions found in a glove box.

2.2 Conclusions about the chemical equilibrium modelling of bentonite porewater

Based on a literature model of porewater in compacted bentonite, a bentonite porewater model was set up and tested against the analysed composition of a porewater in equilibrium with uncompacted bentonite (slurry) that was obtained from the experimental programme. It was considered that the PHREEQC model that was set up gave a good prediction of the literature bentonite porewater model. Subsequent modelling calculations applied the uncompacted bentonite porewater model to the compacted MX-80 bentonite that had been used in the experimental programme.

3 Understanding of the solubility and sorption behaviour of iron

This section describes modelling investigations into the likely precipitation of iron-containing minerals within the bentonite, and the possibilities for sorption of iron onto and within the bentonite under the conditions of interest.

3.1 Understanding the formation of iron-rich solids within compacted bentonite

Experimental evidence (TEM-EDS and total chemical analysis) clearly shows the presence of additional iron within the compacted bentonite samples in contact with the iron wires (wire bentonite samples) after the corrosion process has taken place. One hypothesis suggests that this could be due to precipitation of iron-rich solids, such as magnetite, within the bentonite. A series of model predictions were carried out in compacted bentonite to understand which iron minerals are most likely to form. Note that pyrite was not considered within the bentonite mineral assemblage to prevent any confusion from other sources of iron. The calculations were carried out under (i) a range of reducing and oxidising conditions at a value of pH 8 and (ii) a range of pH values under fixed redox conditions (Eh of –400 mV). These calculations are described in sub-sections 3.1.1 and 3.1.2.

3.1.1 Estimation of the aqueous iron concentration for likely solubility-limiting phases under experimental conditions at fixed pH

The aqueous iron concentration was predicted for five likely solubility-limiting mineral phases. This involved a series of calculations where individual iron minerals were allowed to come to equilibrium with the bentonite porewater, and the predicted concentration of aqueous iron was plotted as a function of redox conditions at fixed pH. The simulations assumed compacted bentonite (1,600 kg dm^{-3} dry density), with cation exchange of major cations and pH buffering by surface complexation of protons, in equilibrium with the artificial groundwater used previously; the pH was around 8.0 and ionic strength ~ 0.64 mol dm^{-3}. The reduction of carbonate to methane gas and sulphate to sulphide was not allowed in the calculations because they were considered kinetically unlikely although thermodynamically feasible. The resulting predictions for aqueous iron concentration due to magnetite, pyrite, haematite, goethite and siderite mineral equilibrations are shown in Figure 3-1 to Figure 3-5. The aqueous iron predictions are plotted as a function of pE. This can be converted to the Eh quantity, with respect to SHE, measured in the laboratory using:

$$Eh(mV) = (pE/1.69) \times 100 \text{ at } 25°C \quad (1)$$

Under reducing condition, iron minerals that contain only Fe(III) are thermodynamically unstable and will transform very slowly to stable solids containing Fe(II). Therefore goethite, haematite (Fe(III)OOH and $Fe(III)_2O_3$ respectively) will be less stable at low Eh than magnetite ($(Fe(II)Fe(III))_3O_4$). Measured redox values taken from the experimental programme shown a steady state Eh value of around –400 mV, corresponding to a pE of around –6.8 (gold and stainless steel Eh electrodes, /2/). From Figure 3-1 to Figure 3-5, pyrite is noted to be the least soluble under reducing conditions (aqueous iron concentration of 5×10^{-7} mol dm^{-3} at pE of –7) with magnetite calculations giving an aqueous iron concentration of 2×10^{-4} mol dm^{-3} at pE of –7. However the Fe(III) containing solids give aqueous iron concentrations of 1×10^{-3} mol dm^{-3} and 2×10^{-3} mol dm^{-3} for haematite and goethite respectively at pE of –7, but would not be

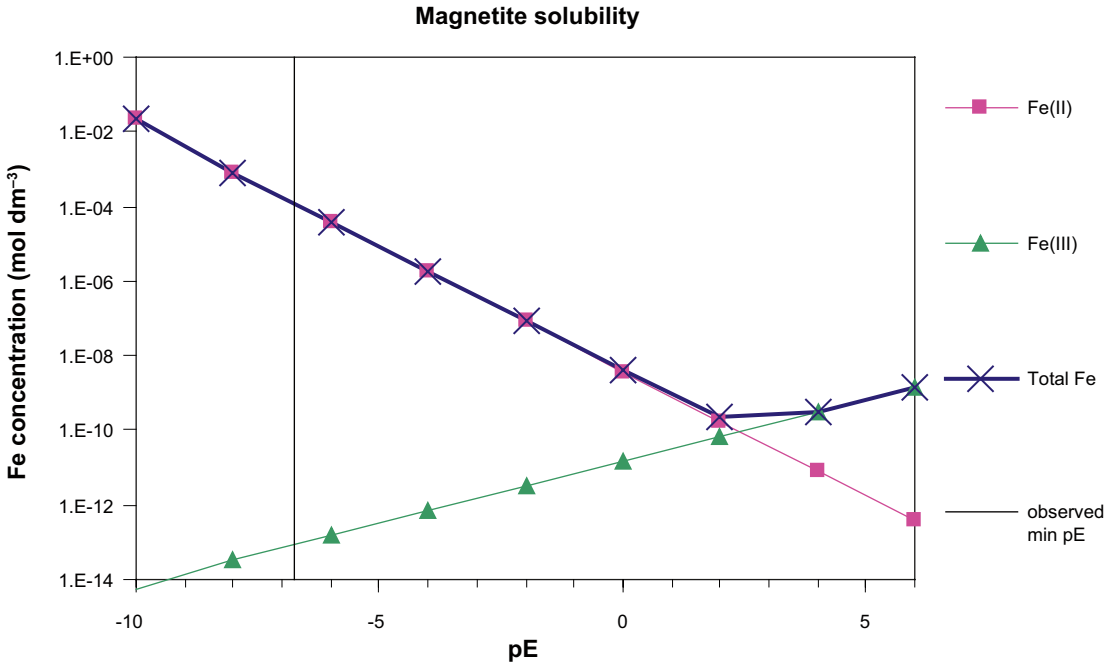

Figure 3-1. *Estimation of the aqueous iron concentration for magnetite as a function of redox condition. Note that reduction of carbonate to methane and sulphate to sulphide transitions were not allowed. The vertical line shows the observed steady state value of Eh in the experimental programme.*

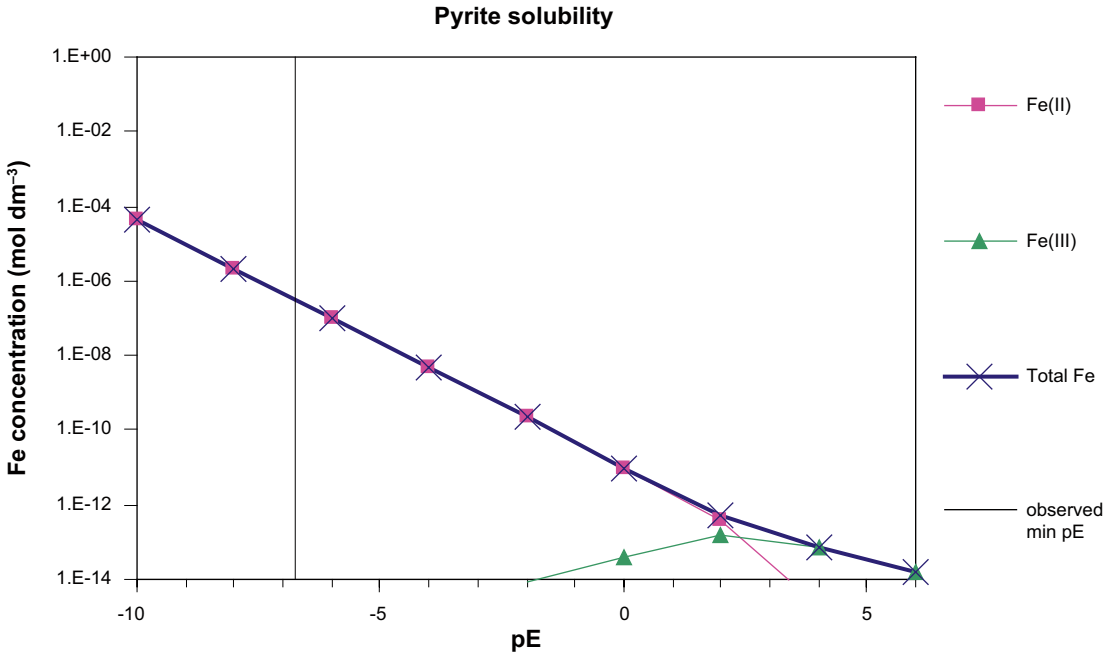

Figure 3-2. *Estimation of the aqueous iron concentration for pyrite as a function of redox condition. Note that reduction of carbonate to methane and sulphate to sulphide transitions were not allowed. The vertical line shows the observed steady state value of Eh in the experimental programme.*

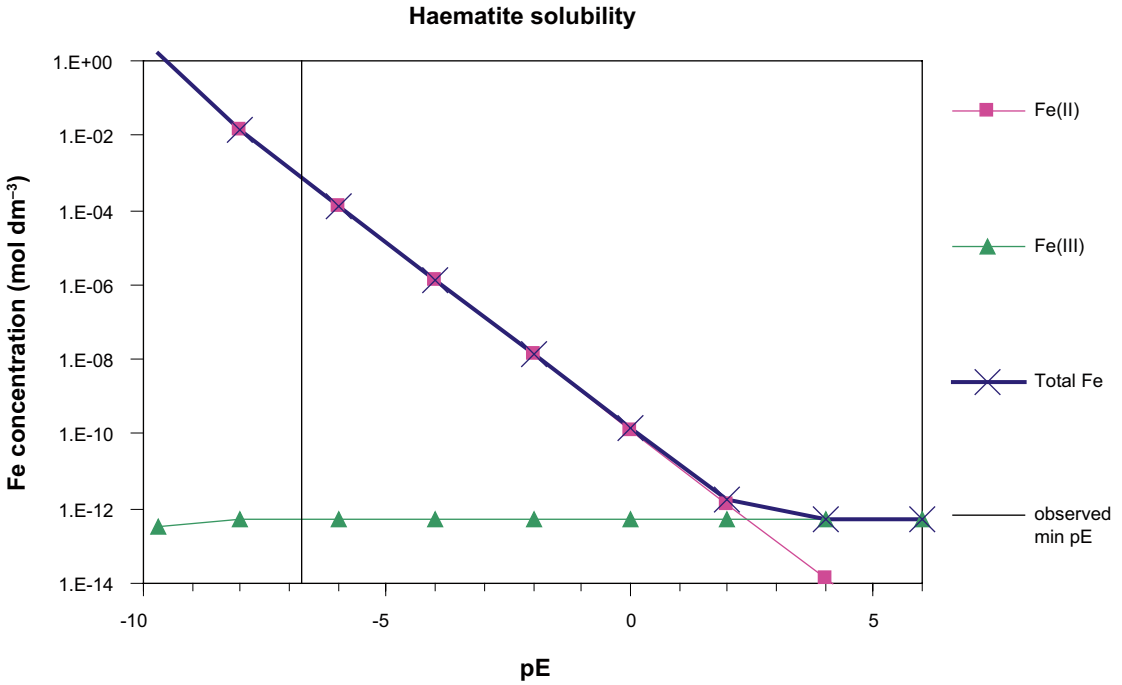

Figure 3-3. *Estimation of the aqueous iron concentration for haematite as a function of redox condition. Note that reduction of carbonate to methane and sulphate to sulphide transitions were not allowed. The vertical line shows the observed steady state value of Eh in the experimental programme.*

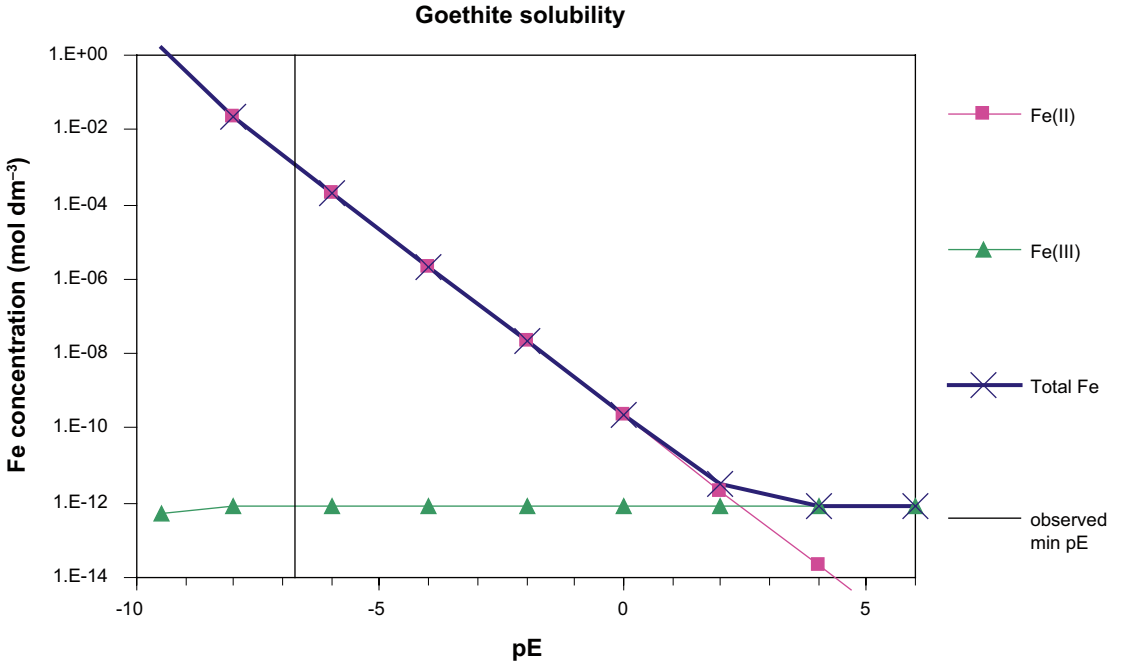

Figure 3-4. *Estimation of the aqueous iron concentration for goethite as a function of redox condition. Note that reduction of carbonate to methane and sulphate to sulphide transitions were not allowed. The vertical line shows the observed steady state value of Eh in the experimental programme.*

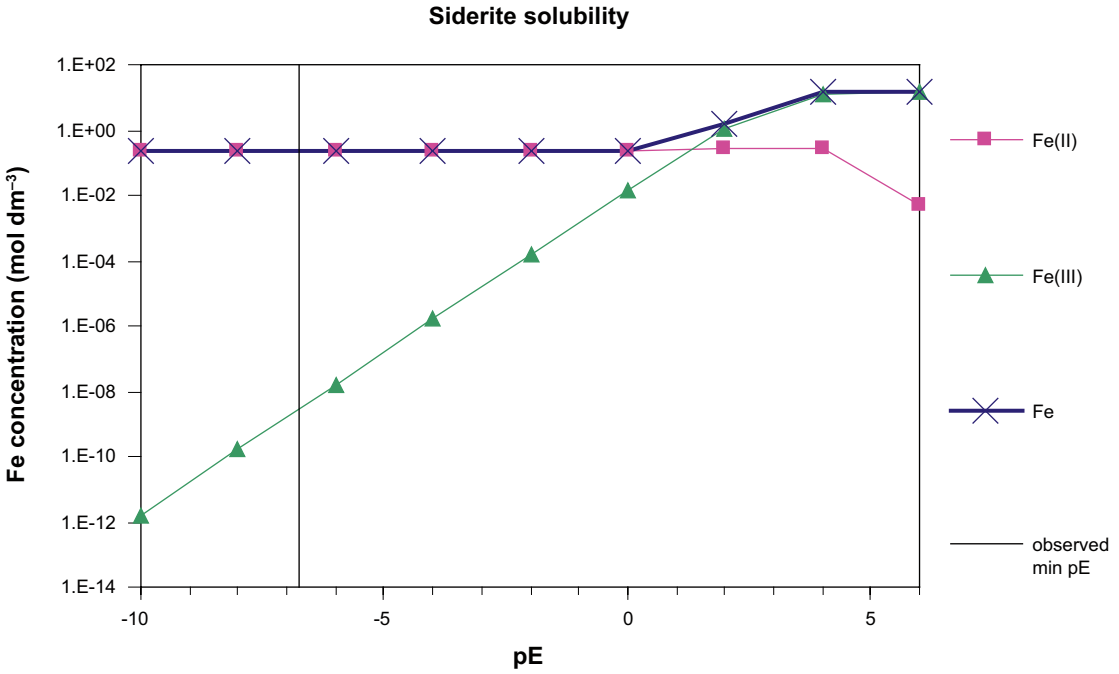

Figure 3-5. *Estimation of the aqueous iron concentration for siderite as a function of redox condition. Note that reduction of carbonate to methane and sulphate to sulphide transitions were not allowed. The vertical line shows the observed steady state value of Eh in the experimental programme.*

expected to form if magnetite precipitation occurred and hence these aqueous iron concentrations can be considered unrealistically high. Similarly, siderite is even more soluble with a predicted aqueous iron concentration of 0.2 mol dm^{-3} at a pE of –7 and carbonate concentration of 0.01 mol dm^{-3}.

At pH 8, magnetite is predicted to be the thermodynamically most stable solubility-limiting phase for the experimental system. A variant calculation was also carried out at pH 8.4 which gave a similar prediction of magnetite as the solubility-limiting phase. Note that if the pH was allowed to float in the model predictions (not fixed), then hydroxyl ions would be consumed as magnetite forms which would affect the pH:

$$Fe^{2+}_{(aq)} + 2Fe^{3+}_{(aq)} + 8OH^{-}_{(aq)} \rightarrow Fe_3O_{4(s)} + 4H_2O_{(l)} \quad (2)$$

(The formation of significant amounts of pyrite requires microbial activity to reduce sulphate present in the system to sulphide and hence pyrite can be excluded as kinetically unlikely to be the solubility-limiting phase.) From these calculations, an estimated aqueous iron concentration of about 2×10^{-4} mol dm^{-3} is predicted at the experimental Eh and pH 8 assuming saturation of magnetite.

3.1.2 Estimation of the aqueous iron concentration for likely solubility-limiting phases under experimental conditions at fixed Eh

Further calculations were carried out for magnetite as the most likely solubility-limiting phase to predict the aqueous iron concentration at varying pH with the redox condition fixed at the experimentally measured value of –400 mV. Other model parameters were consistent with sub-section 3.1.1. $Fe(OH)_{2(s)}$ was also predicted as an alternative, more amorphous, phase that could form from initial corrosion products. For instance, it is considered possible that the solubility control close to the corroding surface would be a surface layer of $Fe(OH)_{2(s)}$, which would then dissolve and release Fe^{2+} ions into solution. The resulting predictions for aqueous iron concentration plotted as a function of pH are shown in Figure 3-6 and Figure 3-7.

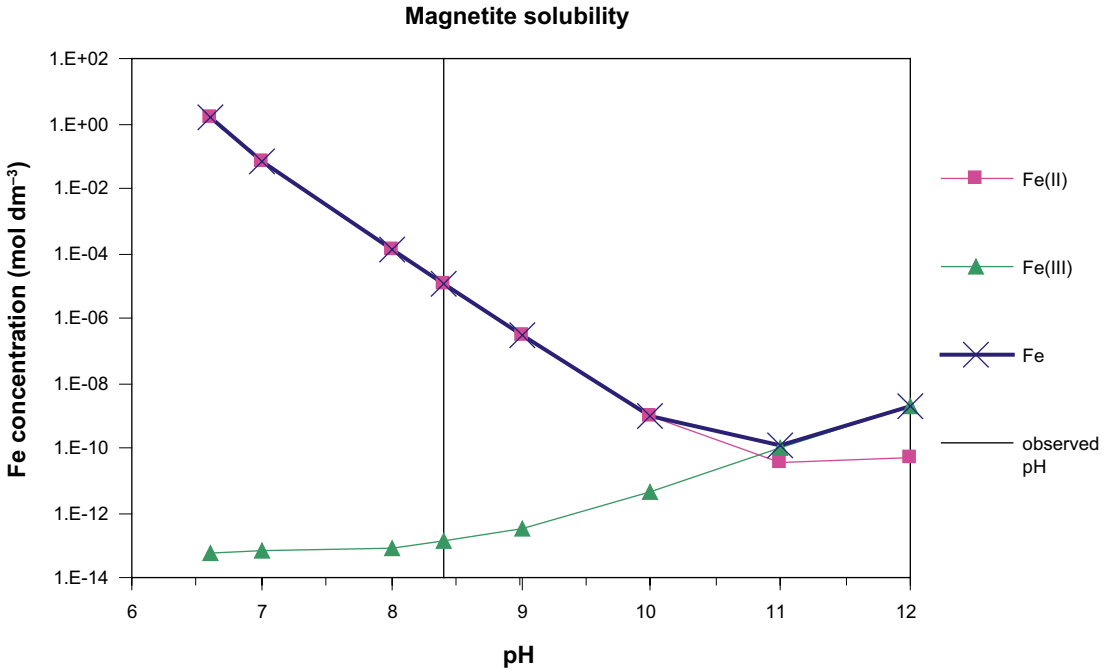

Figure 3-6. *Estimation of the aqueous iron concentration for magnetite as a function of pH. The vertical line shows the experimentally measured pH.*

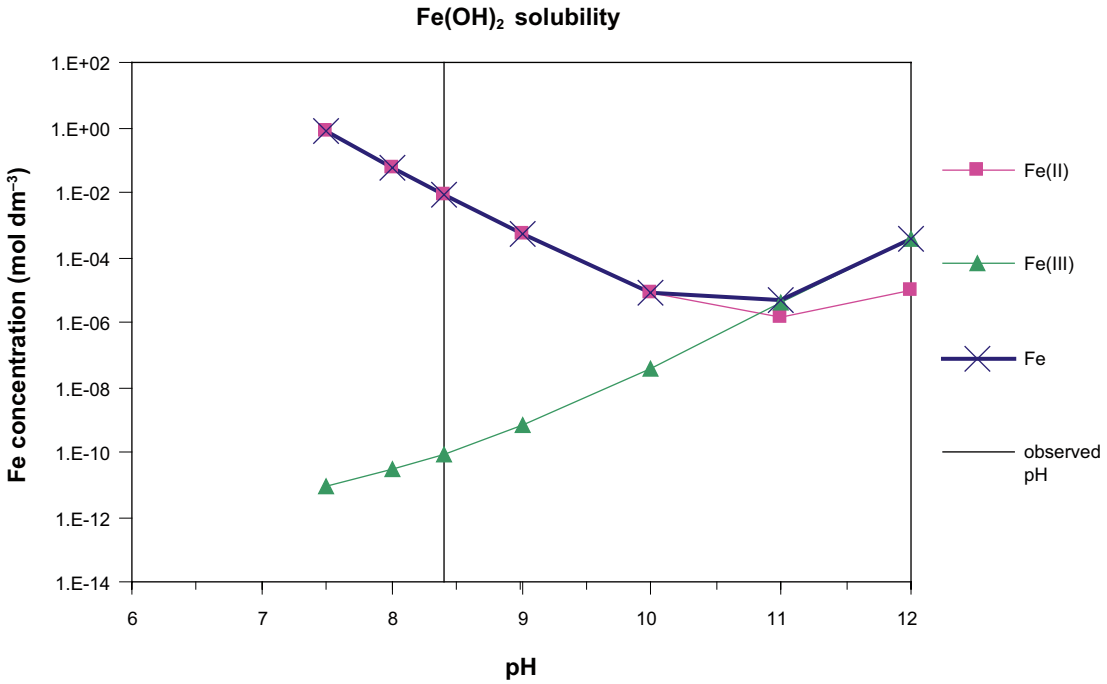

Figure 3-7. *Estimation of the aqueous iron concentration for $Fe(OH)_{2(s)}$ as a function of pH. The vertical line shows the experimentally measured pH.*

The results show that magnetite solubility is not constant between pH 8 to pH 8.4 but varies between an iron concentration of 1×10^{-4} mol dm^{-3} to 1×10^{-5} mol dm^{-3} respectively. At higher pH, the solubility of magnetite is low, about 1×10^{-10} mol dm^{-3} at pH 11.

$Fe(OH)_2$ solubility shows a similar profile but with predicts much higher iron concentrations (1×10^{-4} mol dm^{-3} at pH 8.4) which is consistent with a more amorphous solid.

3.2 Inclusion of iron sorption within the compacted bentonite porewater model

This section describes the development of the compacted bentonite porewater model to include exchange of iron onto clay interlayer sites, and to include the complexation of iron onto surface sites. In earlier sections of this report, the bentonite porewater model looked at major cation exchange and pH buffering by surface complexation processes of H^+, but did not need to include the sorption of iron within the model. The bentonite model was set up for compacted bentonite with dry density of 1,600 kg m^{-3}, assuming 87% montmorillonite and associated sorption sites, under low pCO_2, reducing conditions.

3.2.1 Exchange of iron in the compacted bentonite porewater model

Work carried out by Kamei et al. 1999 /18/, reported a selectivity constant (K) for the exchange of Fe^{2+} onto Na-montmorillonite at low ionic strength (I = 0.05 mol dm^{-3}) and high liquid to solid ratio (50 l/kg). The selectivity coefficient for ion exchange is defined according to the convention in Gaines and Thomas 1953 /19/ and has been included within the compacted bentonite model calculations:

$$2\ \text{Na-montmorillonite} + Fe^{2+} = \text{Fe-montmorillonite}_2 + 2\ Na^+ \qquad \log K = 0.267 \qquad (3)$$

3.2.2 Surface complexation of iron in the compacted bentonite porewater model

The surface complexation constants for the sorption of iron onto surface Na-montmorillonite sites can be estimated using the Linear Free Energy Approach (LFER) of Bradbury and Baeyens 2005 /20/. The LFER approach is based on an earlier Bradbury and Baeyens non-electrostatic sorption model /3/ that is consistent with their bentonite porewater model /4, 5/. Hence it is appropriate to make use of the LFER approach in the current work because we have similarly based our model on the Bradbury and Baeyens bentonite porewater model. They report that a good correlation is found for a wide variety of cations between the logarithms of the strong and weak surface binding constants on Na-montmorillonite and the logarithm of the stability constants for the formation of the corresponding hydrolysis product.

The LFER approach makes use of the straight line correlation between the surface complexation constant for a selected cation and its corresponding hydrolysis equilibrium constant. For instance, if the hydrolysis constant for Fe^{2+} is known, as well as the linear correlation for a selection of similar divalent cations, then the surface complexation constant for Fe^{2+} sorption onto montmorillonite can be neatly estimated. For surface sorption of a divalent cation such as Fe^{2+} onto a weak site, then assuming that the cation is denoted by M, for strong sorption sites (Equation 4) or weak sorption sites (type 1, Equation 5), the general surface binding constant can be written as Bradbury and Baeyens 2005 /20/:

$$\equiv\text{Surfa\_strongOH} + M^{2+} + yH_2O \leftrightarrow \equiv\text{Surfa\_strongOM(OH)}_y^{(1-y)} + (y+1)H^+, \qquad {}^{s}K_y \qquad (4)$$

$$\equiv\text{Surfa\_weakoneOH} + M^{2+} + yH_2O \leftrightarrow \equiv\text{Surfa\_weakoneOM(OH)}_y^{(1-y)} + (y+1)H^+, \ {}^{w}K_y \qquad (5)$$

While in solution, the general hydrolysis constant can be written as:

$$M^{+2} + xH_2O \leftrightarrow M(OH)_x^{(2-x)} + xH^+, \qquad {}^{OH}K_x \qquad (6)$$

Bradbury and Baeyens derive the following fit from their data for sorption onto strong and weak sites (Equations 7 and 8):

$$\log {}^{s}K_{x-1} = 8.1 + 0.9 \times \log {}^{OH}K_x \qquad (7)$$

$$\log {}^{w}K_{x-1} = 6.2 + 0.98 \times \log {}^{OH}K_x \qquad (8)$$

The hydrolysis constants for Fe^{2+} from the HATCHES NEA17 database are:

$Fe^{2+} + H_2O \leftrightarrow FeOH^+(aq)$ $\log_{10}{}^{OH}K_x = -9.5$ (9)

$Fe^{2+} + 2H_2O \leftrightarrow Fe(OH)_2(aq)$ $\log_{10}{}^{OH}K_x = -20.6$ (10)

$Fe^{2+} + 3H_2O \leftrightarrow Fe(OH)_3^-(aq)$ $\log_{10}{}^{OH}K_x = -31$ (11)

To apply the LFER approach, the aqueous phase hydrolysis reactions ($M(OH)_x^{(2-x)}$ for divalent cations) and the surface complexation reactions (Surfa_strong≡$OM(OH)_y^{(1-y)}$ for divalent cations) need to have the same general form with x = y + 1. Therefore, using Equation 7 (strong sites) and the appropriate hydrolysis constant (Equations 9 to 11), the surface complexation constant for Fe(II) sorption onto strong Na-montmorillonite sites can be calculated. The results are shown in Table 3-1. Inclusion of iron surface complexation also requires additional protonation and deprotonation complexation onto strong sites. Hence the surface complexation formation reactions with strong sites are required (Appendix 1).

Similarly, using Equation 8 (weak sites) and the first hydrolysis constant then the surface complexation constant for Fe(II) sorption onto weak Na-montmorillonite sites is shown in Table 3-2.

3.2.3 Investigation of iron sorption as a function of pH

The sorption processes of iron were investigated as a function of pH by including the selectivity coefficient for ion exchange and the surface binding constants for surface complexation with a compacted bentonite model. The system was modelled using:

- 1,600 kg m^{-3} dry density of bentonite (80 kg of MX-80 per litre of porewater).
- Reducing conditions.
- Artificial groundwater used in the bentonite slurry experiments (31.56 g dm^{-3} NaCl and 1.06 g dm^{-3} Na_2CO_3).
- The ionic strength was about 0.6 mol dm^{-3}.
- Prior to sorption taking place, the iron was contained only within the aqueous phase with a concentration of 5×10^{-4} mol dm^{-3} (i.e. 5×10^{-4} total moles of iron were present in the system).
- No mineral equilibrations were included.
- 0.139 moles of strong surface complexation sites per 80 kg of MX-80.
- 2.78 moles of each type of weak surface complexation site per 80 kg of MX-80.

Table 3-1. Estimated equilibrium constants for iron surface complexation reactions with strong sites.

Strong site surface complexation reaction for iron	log $^sK_{x-1}$
≡Surfa_strongOH + Fe^{2+} ↔ ≡Surfa_strongOFe^+ + H^+	–0.45
≡Surfa_strongOH + Fe^{2+} + H_2O ↔ ≡Surfa_strongOFeOH + $2H^+$	–10.4
≡Surfa_strongOH + Fe^{2+} + $2H_2O$ ↔ ≡Surfa_strongO$Fe(OH)_2^-$ + $3H^+$	–19.8

Table 3-2. Estimated equilibrium constants for iron surface complexation reactions with weak sites.

Weak site surface complexation reaction for iron	log $^wK_{x-1}$
≡Surfa_weakoneOH + Fe^{2+} ↔ ≡Surfa_weakoneOFe^+ + H^+	–3.11

- Surface area of 31.3 m^2 g^{-1} montmorillonite.
- Cation exchange capacity of 787 mEq per kg MX-80. Prior to sorption occurring, the ion exchange sites were filled with 53.44 moles of Na, 1.04 moles of K, 1.6 moles of Mg and 2.64 moles of Ca.

The modelled sorption of iron onto MX-80 bentonite was plotted as a function of pH (Figure 3-8) ion exchange sites and surface complexation sites. The sorption distribution coefficient, K_d (dm^3 kg^{-1}) can be calculated from $K_d = F/C$, where F is the amount of iron in the solid phase (kg) divided by the mass of bentonite solid (kg), and C is the amount of iron in the aqueous phase (kg) divided by the volume of solution (dm^3).

Figure 3-8 shows that the sorption of iron by ion exchange is small (0.01% of the total sorbed iron at pH 8) in comparison to the amount of iron sorbed by surface complexation. At pH 8, about 96% of the sorbed iron is on strong surface complexation sites and about 4% of the sorbed iron is on weak surface complexation sites. The model of iron surface complexation shows that the strongly sorbing surface sites dominate, and indeed become more important as the pH increases. Even at high pH, it is noted that unoccupied strong surface complexation sites remain since the trend of Kd increases as pH increases.

The dependence of surface iron sorption with increasing pH results from the proton dependence of iron sorbed onto surface sites (Table 3-1), the protonation/deprotonation of the surface sites and also on the state of the cation hydrolysis in solution. It is noted that in the high pH region, the effect of preserving a constant aqueous iron concentration (by maintaining an iron mineral saturation) would lead to a greater amount of sorbed iron on strong surface complexation sites. The region of interest to the experimental programme is around pH 8.4 with a K_d value of about 5×10^3 dm^3 kg^{-1} A slight flattening of the sorption profile is noted in this region of the Kd–pH curve. As a result of this flatter region, a small change in pH (between pH 8 and pH 9) should not produce a large effect in the amount of iron sorbed.

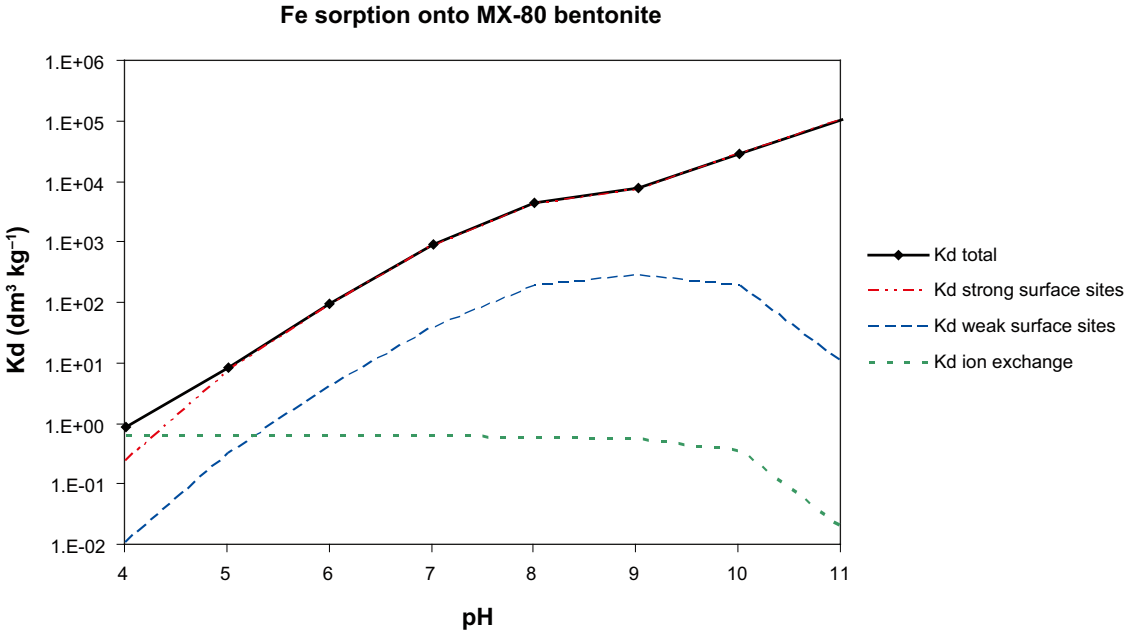

Figure 3-8. *Sorption of iron onto MX-80 bentonite as a function of pH.*

3.3 Calculation of the maximum potential amount of iron sorption by ion exchange and surface complexation

A calculation was carried out to determine the maximum amount of iron that could be sorbed onto bentonite if it is assumed that all surface complexation and ion exchange sites are filled with iron. The maximum potential amount of sorbed iron was then compared with the amount of iron observed on the solid phase. These calculations show that even if all sorption sites were filled by iron, then the maximum amount of sorbed iron (about 2.4 wt % or iron) can not match the observed amount of about 7 wt % iron on the bentonite solid phase.

For instance, if it is assumed that all the surface complexation sites are filled with Fe^{2+} ions, then this gives about 0.2 wt % of sorbed iron for 80 kg of MX-80 (using 2.92 moles of sites per kg of porewater; with sorption onto the strong sites and one type of weak site). In addition, if it is assumed that all the ion exchange sites are filled with Fe^{2+} ions then this gives about 2.2 wt % of sorbed iron (using 63 moles of sites per kg of porewater). These simple calculations do not account for competition of the Fe^{2+} ions with other cations (Na^+, K^+, Mg^{2+} and Ca^{2+} on ion exchange sites) which would reduce any predicted amount of sorbed iron. Alternatively, an increase in pH would increase the sorption of Fe^{2+} onto strong surface complexation sites (Figure 3-8) although the overall number of surface complexation sites would remain constant. Overall, it is considered that the maximum ion exchange and surface complexation capacities can not provide enough iron sorption to match the observed data, and therefore other processes also need to be considered to account for the difference.

For instance, the additional iron observed on the solid phase could also be accounted for by:

- Supersaturation of iron-containing mineral phases which could lead to the formation of solid phases such as magnetite (the thermodynamically most stable solubility limiting phase). Mineral formation could be either by thin layer coatings around montmorillonite grains, or the formation of individual grains. This supersaturation process has been modelled during the transport calculations (section 6.1).
- Substitution of cations within the montmorillonite structure that would lead to the formation of solid solutions of montmorillonite. Although geochemical modelling tends to work with pure phase minerals for simplicity, in practice, minerals of variable composition are common in nature. Solid solutions are permanent ion substitutions within the layers such as replacement of Si^{4+} or Al^{3+} by Fe^{3+}, in contrast to interlayer cations such as Na^+ or Ca^{2+} that are more easily substituted during the ion exchange process. Mineral transformations are considered unlikely to occur at ambient temperatures, and no evidence for the transformation of montmorillonite to an iron-rich clay mineral phase has been observed during the experimental programme.

3.4 Conclusions of the solubility and sorption behaviour of iron

Magnetite was identified as the most thermodynamically stable solubility-limiting phase under the experimental conditions (at about pH 8). Precipitation of pyrite was excluded from the model due to kinetic barriers that would hinder its formation under the experimental conditions and timescale. Further calculations showed that the extent of magnetite formation under fixed redox conditions is dependent on the pH.

An investigation of iron sorption onto MX-80 bentonite showed that surface complexation onto strongly binding surface sites is the predominant form of sorbed iron. In addition, the sorption of iron is pH dependent.

4 The corroding iron source

4.1 Modelling the production of iron ions from the corroding source

A source of iron ions from the corroding source is required for the transport modelling. The source of iron ions is modelled as the first cell, from which diffusion of solutes into subsequent cells takes place. Two approaches were considered to parameterise the iron source term, either (i) dissolution of iron using a kinetically controlled corrosion rate that approximates the measured corrosion rate, or (ii) dissolution of iron mineral phases at thermodynamic equilibrium (for example, magnetite or $Fe(OH)_{2(s)}$ in equilibrium with bentonite porewater would maintain a constant aqueous concentration of iron ions).

4.1.1 Kinetically controlled production of iron

The experimental programme measured the evolution rate of gas resulting from the corrosion of iron /2/. Data was available for compacted bentonite and bentonite slurry at 30°C and 50°C. The cumulative gas evolution for compacted bentonite at 30°C was used to fit the source term data. If it is assumed that the corrosion reaction under anaerobic conditions is:

$$Fe_{(s)} + 2H_2O \rightarrow Fe^{2+} + 2OH^- + H_2(g) \quad (12)$$

then the evolution of one mole of hydrogen gas will give a similar amount of Fe^{2+} ions that will diffuse away from the corroding source.

The gas evolution rate data have been fitted with an exponential fit (section 5.2.3). This has been shown on the plot of cumulative gas evolution against time (Figure 4-1). The exponential fit was used as the source term in the transport calculations for the production of iron. The fitted equation is

$$\text{rate} = a\, e^{-\lambda t} + b \quad (13)$$

where rate is in mol hr^{-1} if $a = 1.79\times10^{-4}$ mol $m^{-2}hr^{-1}$, $b = 1.27\times10^{-5}$ mol $m^{-2}hr^{-1}$, and $\lambda = 6.65\ 10^{-4}$ hr^{-1}. Then the number of moles of iron produced at any one time is calculated within the model by multiplying the rate by the time. (Further details of the fitting of the equation are shown in section 5.2.3).

There are three discontinuities in the measured volumes of gas evolved which leads to uncertainty in the cumulative gas evolution plot. These discontinuities are due to the gas sampling procedure which requires a changeover of liquid within the collection vessel when the capacity has been reached. As a result of these discontinuities, a cumulative plot of gas evolution will show a lower total gas evolution unless the data are corrected. The rate of gas generation against time has been fitted in a parallel study (section 5.2.3) and therefore the cumulative gas evolution data can be amended at specific time points to account for the discontinuities. For instance, at each discontinuity the fitted gas evolution rate has been used to predict the amount of gas evolved that has not been measured. Then this amount of 'missing' gas can be included in the cumulative gas evolution plot which results in an overall increase in the total amount of gas.

The uncorrected data are shown as blue unfilled symbols in the cumulative plot of gas evolution (Figure 4-1), while the corrected data that account for the discontinuities are shown as pink filled symbols. The corrected data have been fitted with two black straight lines equations for the initial and long term gas generation rate (Figure 4-1). The exponential fit of the gas generation rate (calculated in section 5.2.3) is shown as a green line and has been applied in subsequent transport calculations. The exponential fit of the gas generation rate is based on the uncorrected data and therefore shows a lower long term gas generation rate. The differences

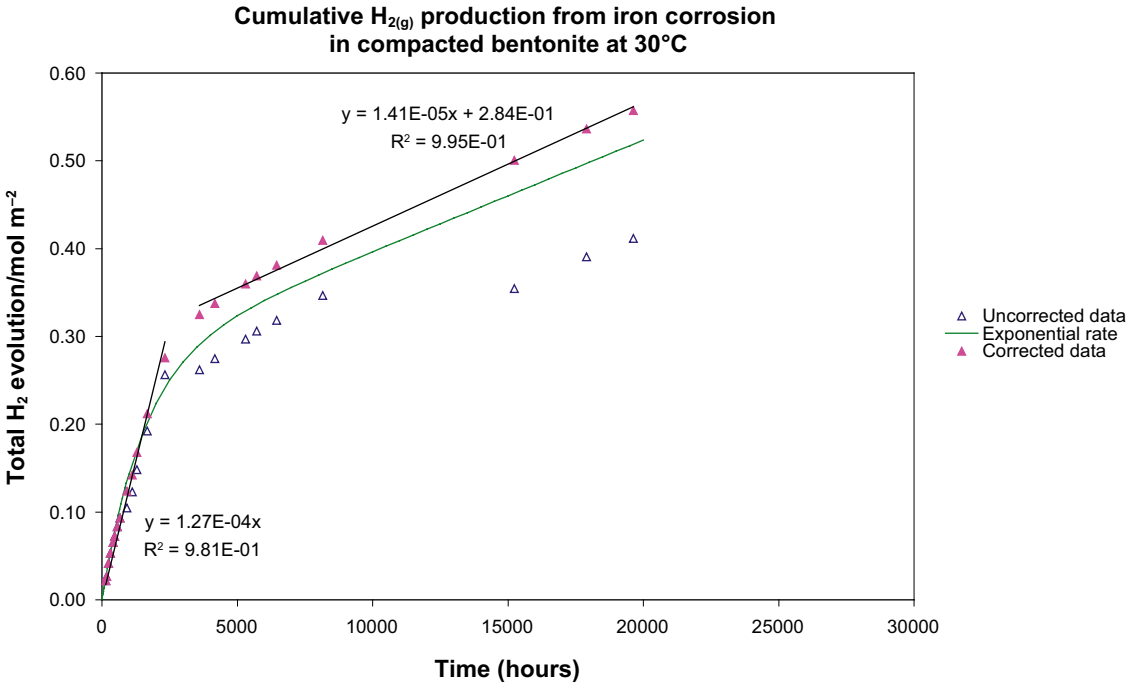

Figure 4-1. *Cumulative gas evolution modelled with an exponential fit for the gas evolution rate (used in the transport calculations), and straight line short term and long term fit.*

in the results of the two model approaches reflect the uncertainty in the experimental data. However, both model approaches indicate that the total gas evolved and the long-term gas generation rate are greater than indicated in the measured data.

4.1.2 Solubility controlled rate of production of iron

An alternative approach to model the production of iron ions is to allow thermodynamic dissolution of an iron-containing mineral which would maintain a constant concentration of iron ions in solution. This assumes that the balance between the corrosion rate and diffusion away from the corroding surface is sufficient to maintain a reasonable concentration of Fe^{2+} ions close to the surface of the steel such that the aqueous phase is supersaturated with respect to Fe^{2+} and forms an initial corrosion product as a surface layer. Although magnetite has been detected experimentally on the wire surface, it is considered possible that the solubility control close to the corroding surface would be a surface layer of $Fe(OH)_{2(s)}$, which would then dissolve and release Fe^{2+} ions into solution. Therefore, $Fe(OH)_{2(s)}$ has been selected as the secondary iron phase controlling the rate of production of iron.

4.2 Mass balance approach for comparison of the production of gas versus the observed increase in iron in compacted bentonite

It is useful to compare the amount of evolved gas against the observed increase in iron in the compacted bentonite. Assuming that one mole of evolved gas equates to the production of one mole of Fe^{2+} ions using the chemical equation in sub-section 4.1.1, then the maximum amount of Fe^{2+} ions that are predicted be present in the bentonite can be compared against the measured amounts of iron observed in the bentonite after the corrosion has taken place.

The amount of gas evolved from each corrosion experiment has been measured for compacted bentonite at 30°C and 50°C. In addition, the total cumulative evolution of gas can be estimated using the fitted gas evolution rate for the compacted bentonite at 30°C. The measured amount of gas evolved is slightly lower than the predicted total amount of evolved gas because of the correction of the data for discontinuities in the measured volumes of gas (section 4.1.1). (Note that the gas evolution rate has not been corrected for the 50°C sample and therefore the measured gas may be slightly lower than the total evolved.) Using these data, the amount of corroded iron can be calculated, and also the percentage of iron wire lost due to the corrosion (Table 4-1). In the case of the compacted bentonite sample cell at 30°C about 4% of the iron wire is lost due to corrosion. Similarly the percentage of iron added to the bentonite can be predicted, and in the case of the compacted bentonite sample cell at 30°C this is about 4.5 wt % with respect to bentonite.

Comparison of these predicted values against the amounts of iron observed in the bentonite after corrosion has taken place shows that more iron is observed in the bentonite than is predicted. For instance Table 4-1 shows that about 6.6 wt % of iron is observed in the compacted bentonite at 30°C after the background measurement has been deducted although only 4.5 wt % of iron is predicted to be present in the bentonite by the measurement of evolved gas. The agreement between the predicted and measured amount of iron is considered reasonable considering the experimental uncertainty in the measured gas volumes, and the analytical uncertainty of iron concentration measurement within the bentonite.

Alternatively, the differences could be accounted for by:

- An underestimation of the amount of gas evolved. For example, anaerobic corrosion may have been taking place from the moment that the iron was compacted, before the collection of evolved gas took place. Note that small quantities of water will remain even within a ‘dry’ bentonite sample
- Alternatively, limited aerobic corrosion may have taken place initially before reducing conditions dominated which would not produce gas: ($4Fe_{(s)} + 3O_{2(g)} \rightarrow 2Fe_2O_{3(s)}$).
- Some amount of evolved gas may remain as dissolved gas in the aqueous phase and therefore would not be collected in the gas phase. Assuming a maximum gas pressure of 2 MPa that had been calculated in section 4 then Henry’s Law can be used to estimate a concentration of gas dissolved in the aqueous phase. Henry’s Law states that:
  $[G] = k_H \times pG$
  where [G] is the aqueous concentration of dissolved gas (mol dm^{-3}), k_H is Henry’s Law constant (7.8×10^{-4} mol dm^{-3} atm^{-1} for $H_{2(g)}$ at 25°C /21/) and pG is the partial pressure of $H_{2(g)}$ in atmospheres. Therefore the amount of gas dissolved in the aqueous phase is about 2×10^{-4} moles (assuming about 13 ml water per sample cell) and would only contribute about an additional 0.01 wt % of iron for compacted bentonite at 30°C. Clearly this is not enough to explain the discrepancy.
- Variability of the measured iron content in MX-80. The iron content of MX-80 prior to corrosion was measured on an independent bulk sample. However, significant variability of the iron content within the MX-80 could lead to an under-estimation of the background reading which would result in a higher observed value for the wt% of iron (i.e. the background measurement is higher than originally thought)
- Other processes have been suggested that could produce Fe^{2+} ions but would not form gas. For instance, the conceptual model of Lantenois et al. 2005 /22/ suggested the reduction of Fe^{3+} contained within the octahedral sites in the bentonite, and oxidation of $Fe_{(s)}$ from the corroding source, could produce Fe^{2+} ions but no concomitant production of gas. E.g. $Fe_{(s)} + 2Fe^{3+}_{(aq)} \rightarrow 3Fe^{2+}_{(aq)}$. However, this conceptual model was formulated for processes occurring at 80°C.

Table 4-1. Comparison of the predicted amount of corroded iron in the solid phase against the observed amount of iron.*

Wire sample	Evolved gas	Predicted iron				Observed iron in bulk bentonite phase /2/
	Total $H_{2(g)}$ (mol per 0.1 m^2 surface area)	$Fe_{(s)}$ corroded (mol)	$Fe_{(s)}$ corroded (g)	% $Fe_{(s)}$ corroded*	Wt % of Fe in bentonite**	Fe wt% minus background***
Compacted bentonite at 30°C	5.2E–02	5.2E–02	2.90	3.87	4.50	6.63
Compacted bentonite at 50°C	8.1E–02	8.1E–02	4.52	6.03	7.00	8.7

* This assumes that 1.34 moles of iron (75 g) is present in the sample cell.

** This assumes that 64.6 g of bentonite was present in the sample cell and that all the corroded iron is found within the bentonite.

*** This is the wt % iron in the samples determined by lithium metaborate fusion. A background measurement of 2.4 wt % of iron in MX-80 was deducted from these observations.

4.3 Conclusions about the corroding iron source

The source of corrosion ions can be modelled by either using a kinetically controlled rate of production of iron ions that has been fitted to the gas evolution rate that results from the corroding iron, or by a thermodynamically controlled rate due to the solubility of an iron-containing mineral such as $Fe(OH)_2$.

The evolved gas data (and therefore the amount of Fe^{2+} ions that are predicted to be present in bentonite) was compared against the increase in iron in compacted bentonite observed by electron microprobe analysis. The agreement is reasonable with 4.5 wt % of iron is predicted to be present in the bentonite by the measurement of evolved gas, and about 6.6 wt % of iron observed in the compacted bentonite at 30°C by electron microprobe analysis.

5 Understanding the consumption of water close to the iron and its implications for gas escape

The corrosion process requires water and produces hydrogen and it is important to understand how this might affect the environment close to the iron. As water is consumed it is possible that desaturation of the bentonite may take place, which then would provide a pathway for the escape of gas away from the corrosion site. Alternatively, if desaturation does not occur, then conventional ideas suggest that significant build up of gas (several MPa pressure) would be required for the gas to force its way through the bentonite. Using available measured experimental data for the corrosion rate and the hydraulic properties of the bentonite, scoping calculations were carried out to investigate whether desaturation is likely to occur. Two models were produced: a local-scale model representing a small region close to one iron wire in bentonite, and a larger-scale model considering gas migration through a segment of a bentonite cylinder from a corrosion experiment.

5.1 Gas migration in bentonite

Before presenting the scoping calculations, it is helpful to provide an overview[1] of the current status of experimental knowledge and understanding of gas migration in bentonite.

Experiments on gas migration in saturated bentonite exhibit the following main features:

- A threshold pressure for gas entry into bentonite. In some cases at least, this breakthrough pressure has been correlated with the swelling pressure.
- Displacement of only small volumes of water from the bentonite by migrating gas.
- After breakthrough, gas flows at pressures below the threshold for initial flow, but flow ceases at pressures above the applied back pressure.
- Changes in porewater pressure and external stresses in response to the applied gas pressure and the creation of gas pathways.

Three possible mechanisms of gas migration in compacted bentonite have been proposed:

- Conventional two-phase porous medium behaviour. To model this type of flow mechanism, concepts of capillary pressure and relative permeability are invoked to relate the gas and water flows and pressures.
- Microfissuring of the clay, in which new porosity is created to accommodate gas flow. This could involve compression of water and squeezing of water from clay particles (consolidation), as well as dilation of the whole sample.
- Macroscopic fracturing of the clay. This is distinguished from microfissuring by the size of the fissures or fractures.

The interpretation of experimental data on gas migration in saturated bentonite in terms of possible transport mechanisms is presently unresolved, although a consensus appears to be developing that gas migration in densely-compacted bentonite is not conventional two-phase flow /23, 24/.

Despite this consensus, it was convenient to use just such a two-phase flow approach in the scoping calculations, which investigate desaturation of bentonite near a corroding wire. It is plausible that at least the gross features of the results obtained will be correct.

[1] A more detailed review is given in /23/ and references therein.

5.2 Scoping calculations

5.2.1 TOUGH2

The scoping calculations were undertaken using TOUGH2. TOUGH2 is a program for simulating coupled fluid and heat flows for multicomponent, multiphase fluid mixtures in porous and fractured media /25, 26, 27/. It was developed by Lawrence Berkeley Laboratories (LBL). In TOUGH2, flow of each phase is modelled using mass conservation and modified forms of Darcy's law with the multiphase nature of the flow taken into account through relative permeability functions. Transport of dissolved gas in the liquid phase and of the liquid vapour in the gas phase is taken into account. The gas phase is taken to be an ideal gas and additivity of partial pressures is assumed. The solubility of the gas is modelled using Henry's law: the solubility is proportional to the partial pressure of the gas. The program includes several equation-of-state models that allow different types of flow to be modelled.

TOUGH2 uses an integrated-finite-volume spatial discretisation with upstream weighting, and fully implicit first-order backward differences for discretisation in time, with an automatic timestep-choice algorithm. The discretised equations are solved using Newton-Raphson iterations to handle the non-linearities and a direct matrix solver.

5.2.2 Bentonite properties

The bentonite was taken to be a porous medium, with a measured total total porosity of 0.42 /28/. Various correlations between the porosity and the permeability of highly compacted bentonite have been proposed /29, 30/, and these predict the effective permeability will be of the order of 10^{-20} m^2. The tortuosity was taken to be 0.01. (de Marsily /31/ quotes this value of tortuosity for gases in highly compacted bentonite.)

The following prescription was used for the characteristic functions of the bentonite. The capillary pressure, p_c, was taken to be of the form introduced by van Genuchten /32/:

$$\text{where } p_c = p_a\left(S_{ew}^{-1/m} - 1\right)^{1-m}, \tag{14}$$

$$\text{and } S_{ef} = \frac{S_f - S_{fr}}{1 - S_{fr}} \qquad f = w, g, \tag{15}$$

p_a is the "apparent" gas entry pressure, which is a constant [Pa],

m is an adjustable parameter (related to the pore size distribution of a porous medium) that controls the shape of the capillary pressure function,

S_f is the saturation of the fluid phase f (w or g) [–], that is the fraction of the pore space occupied by the phase, and

S_{fr} is the residual saturation of the fluid phase f (w or g) [–], that is the saturation below which the phase is immobile.

The residual saturations were taken to be $S_{wr} = 0.25$ and $S_{gr} = 0$, and m was taken to be 0.5. (This characteristic function and these properties are typical of those used to model gas migration in low-permeability clay, e.g. see /33/.) Various correlations between the permeability and the gas entry pressure have been proposed. One such correlation, derived from laboratory experiments on low-permeability samples of limestone, sandstone and dolomite, is /34/:

$$p_a = 1.80 \times 10^{-8}\left(\frac{1}{k}\right)^{0.43} \tag{16}$$

where k is the permeability in m^2 and p_a is the gas entry pressure in MPa. Therefore the apparent gas entry pressure was taken to be 7 MPa. (This is slightly lower than the expected swelling pressure, which is about 10 MPa.)

The relative permeability functions also were taken to be of the form suggested by the van Genuchten model /32/:

$$k_{rw} = S_{ew}^{\eta}\left[1-\left(1-S_{ew}^{1/m}\right)^{m}\right]^{2}, \text{ and} \tag{17}$$

$$k_{rg} = S_{eg}^{\varsigma}\left[1-\left(1-S_{eg}^{1/m}\right)\right]^{2m} \tag{18}$$

where η, ζ are adjustable (pore connectivity) parameters for the water and gas phases respectively. The van Genuchten model suggested that values of 0.5 would be typical of porous media and these values were used in the calculations.

5.2.3 Gas generation rate

The gas generation rate and the water consumption rate are important inputs to the scoping calculations, and were obtained by calculating a best fit to experimental data on the corrosion of iron wire embedded in compacted bentonite at 30°C /2/.

The data for the gas generation rate were fitted to an exponential of the form

$$rate = ae^{-\lambda t} + b \tag{19}$$

where $a = 1.79\ 10^{-4}$ mol $m^{-2}hr^{-1}$, $b = 1.27\ 10^{-5}$ mol $m^{-2}hr^{-1}$, and $\lambda = 6.65\ 10^{-4}$ hr^{-1}. A plot showing the experimental data[2] and the fitted curve is shown in Figure 5-1.

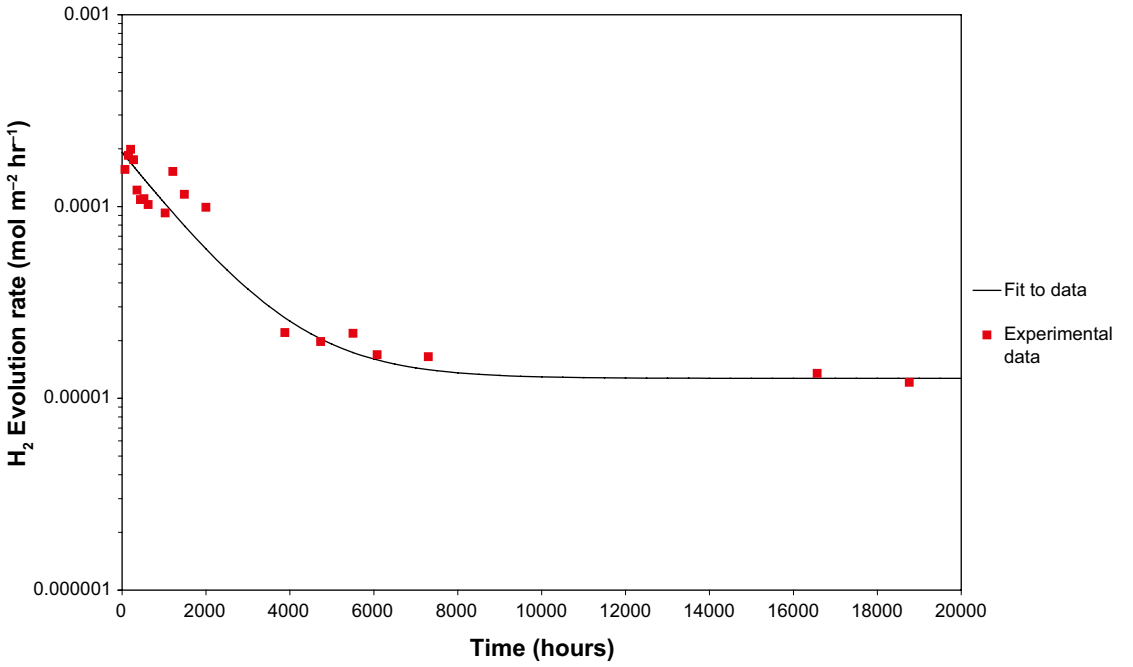

Figure 5-1. *Curve fitted to 30°C iron wire in compacted bentonite experimental data.*

[2] Data at those times when the 'reservoir' in the experiment was refilled were excluded from the analysis, because the perturbation appeared to lead to consistently lower corrosion rates.

The water consumption rate is just twice the hydrogen gas generation rate, as

$$Fe_{(s)} + 2H_2O_{(l)} \rightarrow H_{2\,(g)} + Fe(OH)_{2\,(aq)} \quad (20)$$

5.3 Local-scale model

A model was set up to represent gas migration in a small region close to one iron wire embedded in bentonite. The model region is shown in Figure 5-2, and a blown-up section of the grid close to the iron wire, at x = 0, is shown in Figure 5-3.

Note that:

- The wire itself is not explicitly modelled.
- There is a small void space between the wire and the bentonite, shown as the red element in Figure 5-3.
- The bentonite, shown as the black elements, is modelled along a one-dimensional section which is normal to the wire and extends to a point halfway to a nearby wire.

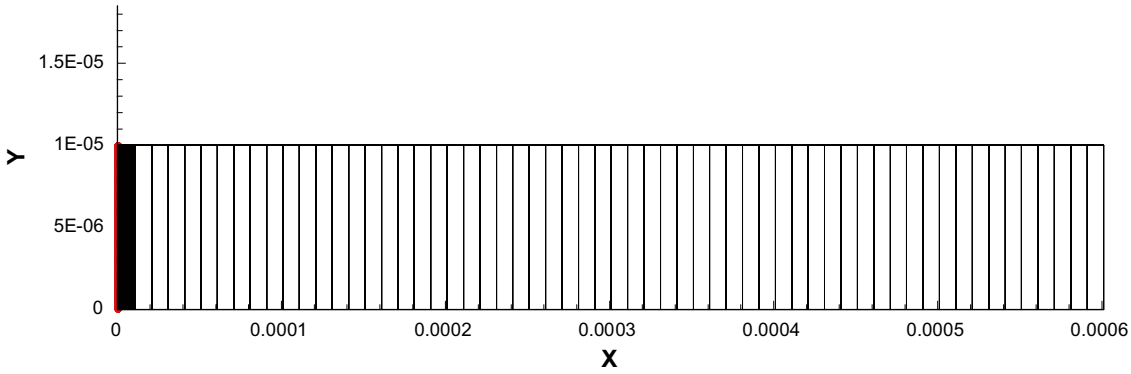

Figure 5-2. *Grid for the local-scale model.*

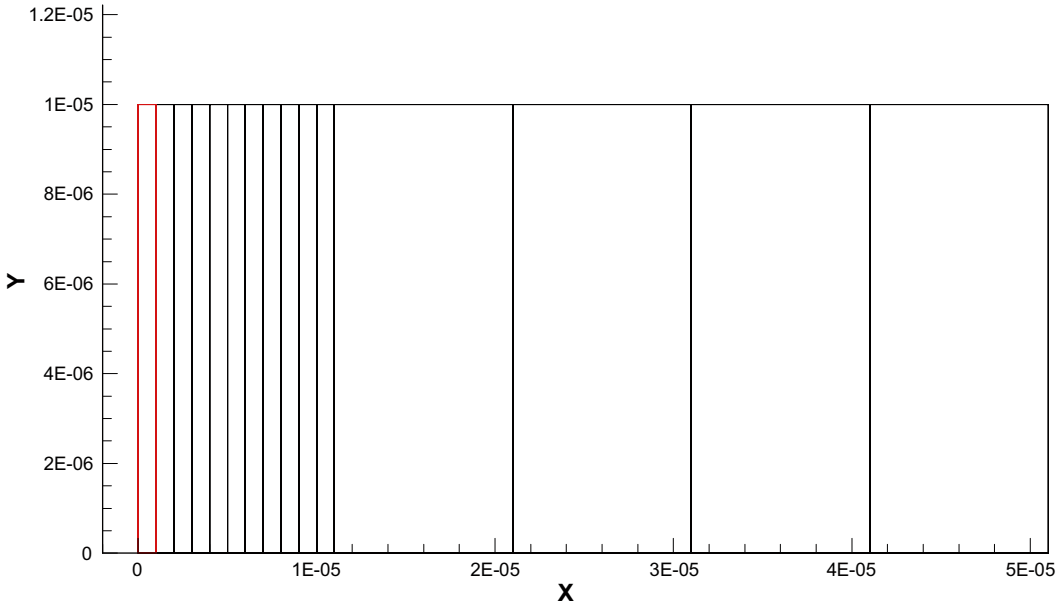

Figure 5-3. *Section of the local-scale model grid close to the iron wire (x = 0).*

5.3.1 Initial and boundary conditions

Initially the void space was taken to be gas filled, the bentonite was taken to be fully water saturated and the pressure throughout the model was 1 atmosphere.

The gas generated by corrosion of the iron wire was injected into the void space between the wire and the bentonite, and the water consumed was removed from the adjacent cell (in the bentonite).

On all of the boundaries of the model, except for the outer boundary at $x = 6\times10^{-4}$ m, no flow boundary conditions were set. A constant pressure of 1 atmosphere was set on the boundary at $x = 6\times10^{-4}$ m to allow gas to escape from the model.

Temperature variations were neglected, and the temperature was taken to be 30°C.

5.3.2 Results of the calculation

The pressure in the void space increases as gas is generated, and as a result gas begins to migrate into the bentonite. The gas is able to go into solution and escape from the model by diffusion. This process occurs to such an extent that there is not a significant increase in gas pressure; the pressure remains lower than the apparent gas entry pressure of the bentonite (7 MPa). Also, the bentonite close to the wire is not significantly desaturated due to corrosion of the wire.

5.4 Larger-scale model

A further model was set up to investigate gas migration on the experimental scale /2/. Each corrosion experiment holds a cylindrical sample of bentonite, the properties of which are given in Table 5-1.

A segment of the bentonite cylinder was modelled; the model grid is shown in Figure 5-4. The grid is refined towards the outer boundary, because it is there that there might be large changes in the variables such as pressure.

Corroding iron wires were assumed to be distributed equally throughout the bentonite so the gas generation rate was distributed evenly through the model.

5.4.1 Initial and boundary conditions

As in the local scale model, the bentonite was taken to be fully water saturated initially and at a pressure of 1 atmosphere.

Gas was injected into each element and water was removed from each element at a rate distributed evenly in space.

Table 5-1. Properties of the bentonite sample used in 30°C iron wire experiment.

Parameter	Value
Radius	0.014 m
Height	0.07 m
Volume	4.3×10^{-5} m^3
Total surface area of wire	0.1 m^2

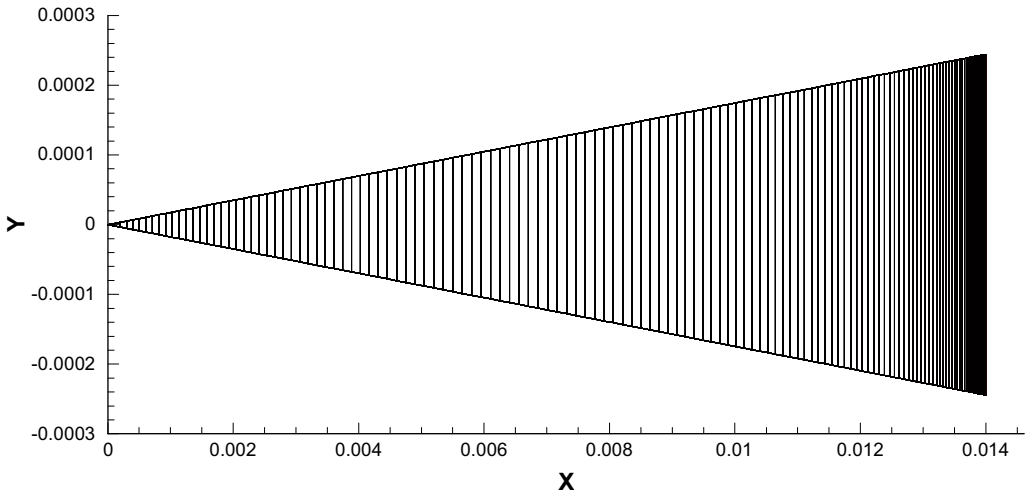

Figure 5-4. *Grid for the larger-scale model.*

The outer boundary, at x = 0.014 m, was held at gas saturation close to 1 and atmospheric pressure. On all other boundaries of the model, no flow boundary conditions were set.

Temperature variations were neglected, and the temperature was taken to be 30°C.

5.4.2 Results of the calculation

Plots showing the pressure, gas saturation and mass fraction of dissolved gas at 20,000 hours (approximately the duration of the corrosion experiments) after gas generation begins are shown in Figure 5-5, Figure 5-6 and Figure 5-7 respectively.

The pressure in the bentonite increases as gas is generated. The pressure peaks at around 2 MPa, which is less than the apparent gas entry pressure of the bentonite (7 MPa), before decreasing to a steady-state with a maximum overpressure of about 1 MPa (see Figure 5-5).

The gas saturation of the bentonite increases as gas is generated and water is consumed due to corrosion of the iron wires. Once the bentonite is no longer fully water saturated gas is able to escape from the bentonite. The gas saturation for the gas to be able to escape is about 1% (see Figure 5-6). The bentonite in the model is not significantly desaturated.

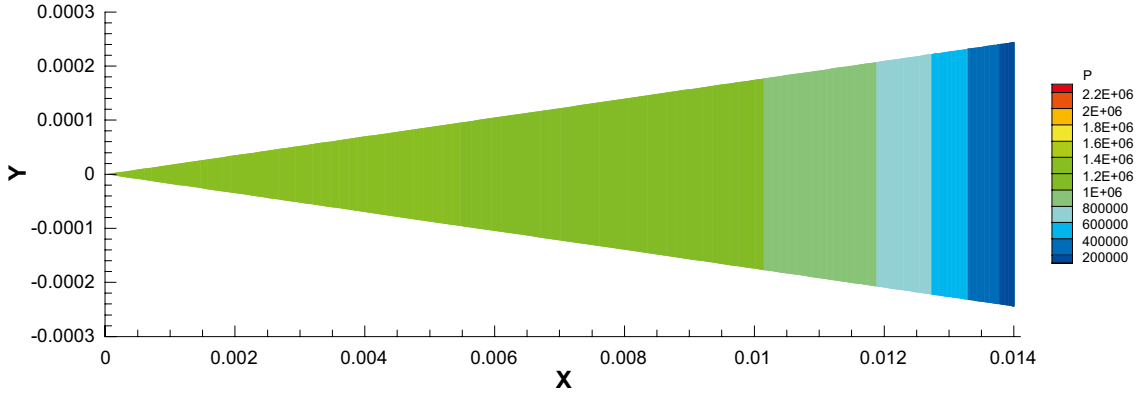

Figure 5-5. *The pressure in the bentonite at 20,000 hours (833.3 days) after gas generation begins.*

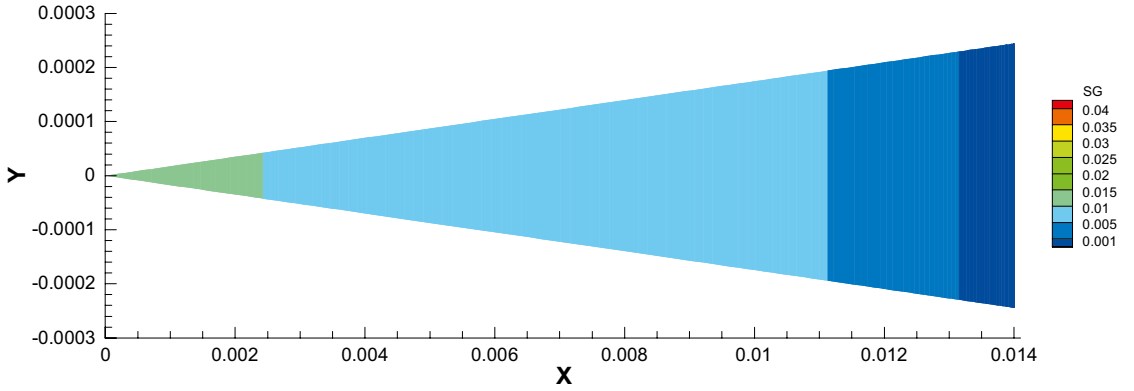

Figure 5-6. *The gas saturation in the bentonite at 20,000 hours (833.3 days) after gas generation begins.*

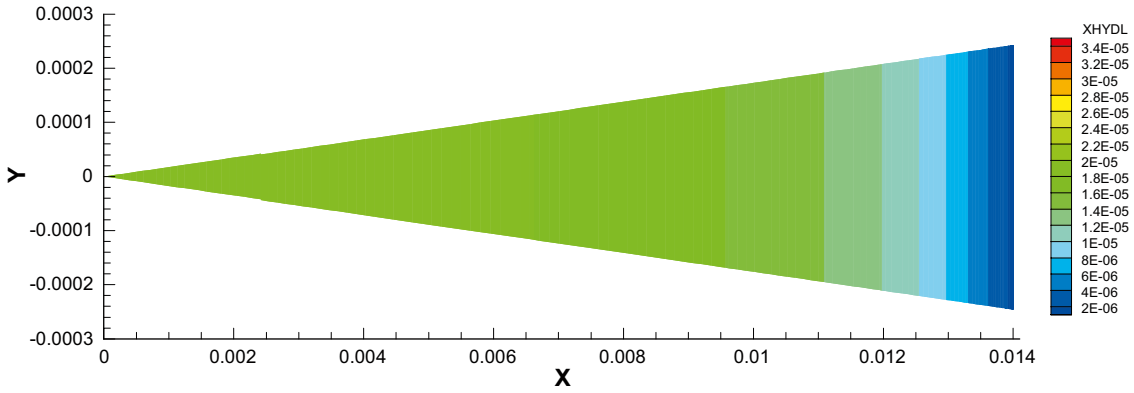

Figure 5-7. *The mass fraction of dissolved gas in the bentonite at 20,000 hours (833.3 days) after gas generation begins.*

5.5 Conclusions of the gas migration models

Two models were set up to investigate whether desaturation of the bentonite is likely to occur, providing a pathway for gas to escape away from the corrosion site.

The local-scale model suggests that:

- On a length scale comparable to the separation of the wires in the bentonite, gas is able to diffuse sufficiently rapidly in solution that there is not a significant increase in gas pressure.
- The bentonite close to the wire is not significantly desaturated due to corrosion of the wire.

The larger-scale model suggests that:

- The gas pressure has a peak of around 2 MPa, which is less than the apparent gas entry pressure of the bentonite (7 MPa), before decreasing towards a steady-state with a maximum overpressure of about 1 MPa.
- If the bentonite is not fully water saturated, then gas is able to escape from the bentonite (the gas saturation for gas to escape is about 1%).
- The bentonite is not significantly desaturated due to corrosion of the iron wires.

6 Modelling the transport of iron through compacted bentonite

The first stages of this work considered modelling of the porewater within compacted bentonite, the likely iron solubility-limiting phases, and the sorption of iron to the solid phase. This understanding was required as basic building blocks before consideration was given to the transport of iron through compacted bentonite, away from the corroding source. This section details the efforts that were made to model the iron transport using a one-dimensional transport model with chemical reactions occurring simultaneously.

6.1 Modelling the transport of iron through compacted bentonite

A one-dimensional transport model was built up in PHREEQC from the various 'building blocks' that have been described above. After production of iron ions from the source cell (section 4.1), the iron was allowed to diffuse through the ten subsequent bentonite cells. Ion exchange and surface complexation was permitted within each of the bentonite cells which would allow sorption of iron onto and within the bentonite solid (section 3.2.1 and section 3.2.2). The pH was buffered by allowing protonation and deprotonation of the surface sites of the bentonite solid (Appendix 1, Table A2 and Table A3). Ion exchange of the major cations, in addition to iron, was also permitted (Appendix 1, Table A4).

6.1.1 Approach taken for modelling the transport of iron through compacted bentonite

The model allowed Fe^{2+} ions to diffuse away from the source cell into the subsequent bentonite cells. Sorption (ion exchange and surface complexation) of the Fe^{2+} was included but mass balance calculations showed significantly lower maximum amounts of sorbed iron could be predicted on the solid phase than observed (section 3.3). The amount of iron observed in the bulk solid phase is about 6.3 wt % iron in the '30°C compacted wire' bentonite samples determined by lithium metaborate fusion (after subtraction of a background measurement of 2.4 wt %. Also, a maximum of 7.5 wt % of iron has been analysed by EMPA close to the corroding wire in a similar sample (Figure 1, Figure 2 /2/).

Several suggestions were considered to increase the amount of iron predicted on the solid phase. Firstly, the sorption capacity could be increased by increasing the ion exchange selectivity coefficients or the surface complexation coefficients which would increase the number of sorption sites filled by iron. However, this relies on there being a sufficient number of total sorption sites and it was calculated that even if the maximum number of sorption sites were filled then this would not account for the maximum amount of iron observed in the solid phase (section 3.3). As a result, any increase in the ion exchange selectivity coefficients and surface complexation coefficients cannot give a sufficient increase in the predicted amount of sorbed iron to match the observations.

Secondly, the supersaturation of iron containing minerals was considered within the modelling. For instance, magnetite (Fe_3O_4) was allowed to precipitate within the bentonite cells when sufficient iron had built up in the aqueous phase to predict supersaturation. It is useful to estimate the thickness of a surface coating of an iron containing mineral to see if mineral

precipitation is a practical proposition given porosity considerations. Assuming a surface area of montmorillonite grains of 31.3 $m^2\ g^{-1}$, a bulk observed iron distribution of 6.6 wt % (Table 4-1), and a density of magnetite of 5.2 g cm^{-3}, the predicted thickness of magnetite was calculated to be about 5×10^{-10} m (5 Å). This value is considered to be a reasonable thickness of mineral that should not significantly reduce the mineral porosity.

Thirdly, the diffusion coefficient was slowed by one order of magnitude (in a variant case). This reduces the transport of Fe^{2+} away from the corroding source, thereby causing an increased concentration of aqueous iron near to the corroding source. As a consequence this is expected to increase the extent of supersaturation of iron containing minerals close to the corroding source and also increase the sorption of iron onto the solid phase.

Fourthly, the effect of pH resulting from the corrosion process was considered. In the case of both types of modelled source cell (kinetically controlled rate of Fe^{2+} production and the solubility limited $Fe(OH)_{2(s)}$), hydroxyl ions are formed which will lead to an increase in pH. An increase in pH will lead to increased sorption onto strong surface complexation sites within the bentonite (Figure 3-8). Similarly, an increase in pH will reduce the solubility of magnetite (Figure 3-6). For instance under the experimental conditions, if the pH was increased to pH 9 then an aqueous iron concentration of only 3×10^{-7} mol dm^{-3} is required before supersaturation of magnetite occurs. In contrast, if the pH remains at pH of 8.4, then an aqueous iron concentration of 1×10^{-5} mol dm^{-3} is required before magnetite supersaturation occurs.

6.1.2 Transport model input parameters

The base case was modelled with a kinetically controlled rate of iron production, a diffusion coefficient of $1.2\times10^{-10}\ m^2\ s^{-1}$ and the possibility of supersaturation of iron containing minerals in bentonite cells. Three variant cases were carried out, using the base case parameters except with (i) an iron source cell containing a saturated solution of $Fe(OH)_{2(s)}$, (ii) a slower diffusion coefficient of $1.2\times10^{-11}\ m^2\ s^{-1}$, and (iii) a more dilute bentonite porewater chemistry.

The transport model input parameters are summarised below:

- Each bentonite cell was assumed to have a cell length of 60 μm, so that the ten model cells give a similar overall length to the iron profile. This matches the ~ 600 μm distance of the iron profile, from the corroding wire to background iron concentrations.
- One litre of porewater was assumed to be present in each model cell.
- The amount of MX-80 solid in each cell was calculated to be 80 kg by assuming one litre of porewater, a liquid to solid ratio of 0.0125 $dm^3\ kg^{-1}$ /8/ and knowing that the bentonite dry density is 1,600 kg m^{-3} /2/. Note that the very low ratio of porewater to solid is based on the amount of free porewater available following the Bradbury and Baeyens approach /8, 9/, (Appendix 1).
- Assuming 80 kg of MX-80 solid containing 87% montmorillonite, 2.78 moles of each type of weak surface site and 0.139 moles of strong surface sites were calculated by using a surface site capacity of 4×10^{-2} mol kg^{-1} for weak sites and of 2×10^{-3} mol kg^{-1} for strong sites /8/.
- The bentonite surface complexation sites in each cell were pre-conditioned to pH 8.4.
- A N_2 BET specific external surface area of 31.3 $m^2\ g^{-1}$ is assumed /8, 35/.
- The iron source cell was set up with either a kinetically controlled rate of production of iron (section 4.1.1), or a solubility controlled equilibrium between $Fe(OH)_{2(s)}$ and the porewater (section 4.1.2). In the case of the kinetically controlled rate of production of iron, the exponential equation and constants are given in section 4.1.1.
- The area of the iron wire was calculated to be 124 m^2 in contact with 1 litre of porewater by assuming an iron wire surface area of 0.1 m^2 /2/ per 64.6 g of bentonite that is present

in the experimental container /36/ and a ratio of 'free' porewater to bentonite solid of 0.0125 $dm^3\ kg^{-1}$ /8/.

- The initial amount of iron available for corrosion was calculated to be about 1,660 moles in contact with 1 litre of porewater and 80 kg MX-80 bentonite (assumes 75 g of steel per experimental container holding 64.6 g of bentonite /36/). Note that the assumed solid to liquid ratio is critical both for the aqueous concentration of Fe^{2+} ions in the source cell and the predicted amount of iron sorbed onto the solid phase. In this case, the 'free' porewater to bentonite solid ratio has been used, which is very low. (An alternative would be to use the total water filled porosity (~ 0.42) comprising the free water, double layer water and inter-layer water. This would correspond to a much higher liquid to solid ratio of 0.207 $dm^3\ kg^{-1}$.)
- Each mole of $Fe_{(s)}$ formed by the kinetic rate equation will then react with water to produce one mole of each of Fe^{2+} ions and H_2 gas, and will release two moles of OH^- (i.e. $Fe_{(s)} + 2H_2O_{(l)} \rightarrow Fe^{2+}_{(aq)} + 2OH^-_{(aq)} + H_{2(g)}$). There is little barrier to the thermodynamic production of iron ions in solution from $Fe_{(s)}$ because the equilibrium constant for this reaction is very small (10^{-12}). Clearly, the production of iron ions will also provide an increase of the pH in the source cell because OH^- ions are formed, and the effect of this needs to be monitored in subsequent bentonite cells.
- To simplify the system, the equilibrated bentonite porewater resulting from mineral equilibrations was not considered in the transport calculations. Instead, the concentration of each aqueous ion contained in the bentonite cells was set using the analysed bentonite porewater (column 1 of Table 2-3, ionic strength of 0.7 mol dm^{-3}).
- Supersaturation of iron-containing minerals (magnetite and iron hydroxide ($Fe(OH)_2$) was permitted within each bentonite cell which could lead to the formation of these minerals. However in practice only magnetite, which is thermodynamically more stable than $Fe(OH)_2$, would be predicted to form. Note that a limitation of the PHREEQC modelling means that supersaturation of iron containing minerals will only occur within the first bentonite cell (Cell 2). For instance, prediction of aqueous iron concentrations greater than the magnetite saturation index within the first bentonite cell will give rise to the formation of magnetite. However, the aqueous concentration of iron that is transported to the second bentonite cell will remain at saturation, and therefore no further magnetite will be predicted to form in the second or subsequent bentonite cells.
- The redox conditions were fixed at the measured value of Eh of –400 mV.
- At the start of the calculation, the ion exchange sites were filled with the major cations (Na, K, Mg and Ca) in the proportions observed in the literature /8, 9/ (Appendix 1, Table A1). Clearly, the cation loadings will change slightly during the calculation as exchange sites come into full equilibrium with the measured aqueous porewater. Note that the measured cation exchange capacity is similar to that observed for MX-80 bentonite in the literature (787 mEq kg^{-1}, or 63 moles of ion exchange sites per 80 kg of bentonite).
- The intrinsic diffusion coefficient for iron in bentonite was estimated in the literature to be similar to that for tritium ($1.2\times10^{-10}\ m^2\ s^{-1}$ /37/) and this value was used in the base case model. However, it was recognised that there is significant uncertainty with this diffusion coefficient and a variant case was carried out using a value of one order of magnitude lower, i.e. $1.2\times10^{-11}\ m^2\ s^{-1}$. Only diffusive transport of each ion was allowed, with no advection of the porewater.
- The stable timestep for pure diffusion can be calculated from $\Delta t \leq (\Delta x)^2/(3 \times Di)$ where Δt is the timestep (seconds), Δx is the cell length (metres) and Di is the diffusion coefficient ($m^2\ s^{-1}$) /3/. For instance, if a diffusion coefficient of $1.2\times10^{-10}\ m^2\ s^{-1}$ is used, the calculation required a timestep of 30 seconds. Given that these experiments were carried out over about 829 days, the resulting modelling runs required a substantial amount of computer time (up to 4 days).
- All calculations were carried out at 25°C.

6.1.3 Model results and discussion

The base case model

The aqueous concentration of iron and the pH predicted in each cell as a function of time for the base case model is shown in Figure 6-1 and Figure 6-2. The aqueous concentration of Fe^{2+} in the source cell (cell 1) follows the kinetic rate equation with initially higher concentrations at early times followed by lower concentrations at later times as the rate of production of, and therefore $Fe^{2+}_{(aq)}$, is reduced.

As the simulation proceeds, the ions contained within the source cell diffuse into the bentonite cells (Cell 2 to Cell 11). Within the bentonite cells, the aqueous iron is able to sorb by ion exchange and surface complexation, and also to precipitate iron-containing minerals if super-saturation is reached. Later paragraphs demonstrate that sorption of iron onto the solid phase is predicted to be a minor part of the overall observed increase of iron within the solid phase.

Figure 6-1 shows that the aqueous concentration in the first bentonite cell (Cell 2) increases at very early times (up to a day), before saturation of magnetite is reached and the aqueous iron concentration is determined by the magnetite solubility. As the simulated experiment proceeds, the aqueous iron concentration in the first bentonite cell reduces slowly with time as the predicted pH increase slightly, which affects the magnetite solubility. The aqueous iron concentrations in the remaining bentonite cells (Cells 3 to 11) are dependent on diffusion from cell 2 and therefore are also limited by the magnetite solubility. Two main ionic species make up the total aqueous iron concentration in all bentonite cells, consisting of about half $FeCl^{+}_{(aq)}$ and half $Fe^{2+}_{(aq)}$.

The pH in each cell as a function of time is shown in Figure 6-2. The pH of the source cell increases at very early times (up to 1 day) due to the production of OH^- ions as the iron wire corrodes (equation 11). Subsequently, the production of OH^- ions in the source cell is outweighed by diffusion away from the corroding source and the pH reduces. In the bentonite

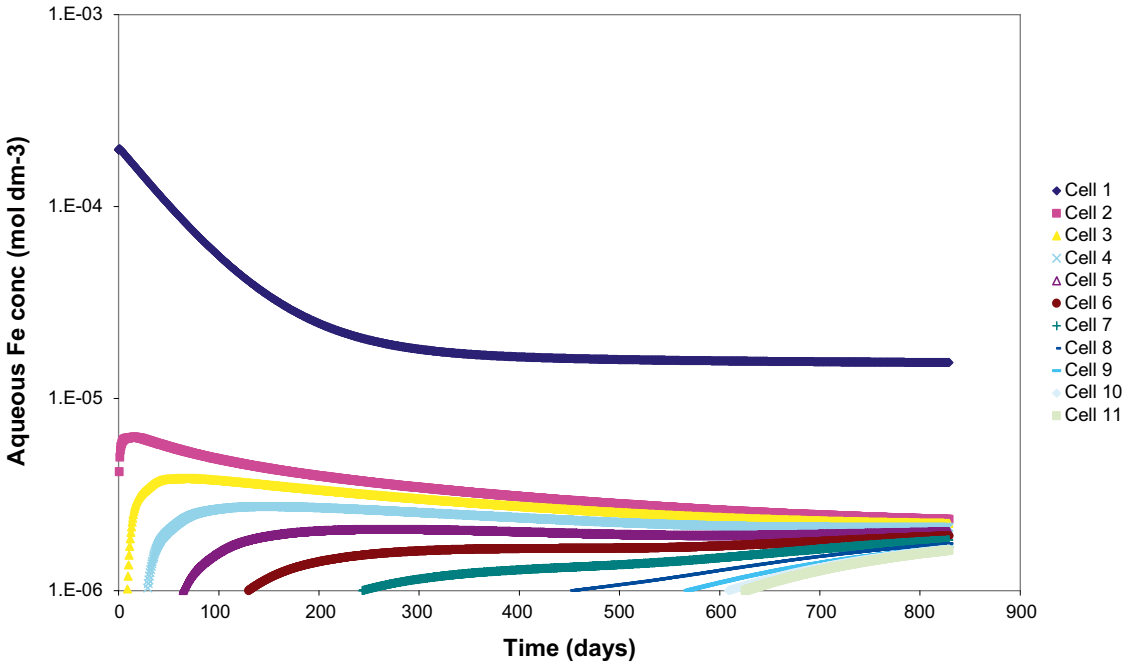

Figure 6-1. *Modelled aqueous concentration of Fe^{2+} ions as a function of time resulting from the corrosion of iron wire. The source term was modelled by fitting experimental gas evolution rate data (Cell 1) and diffusion into the surrounding bentonite (Cell 2 to Cell 11). A diffusion coefficient of 1.2×10^{-10} m^2 s^{-1} was used.*

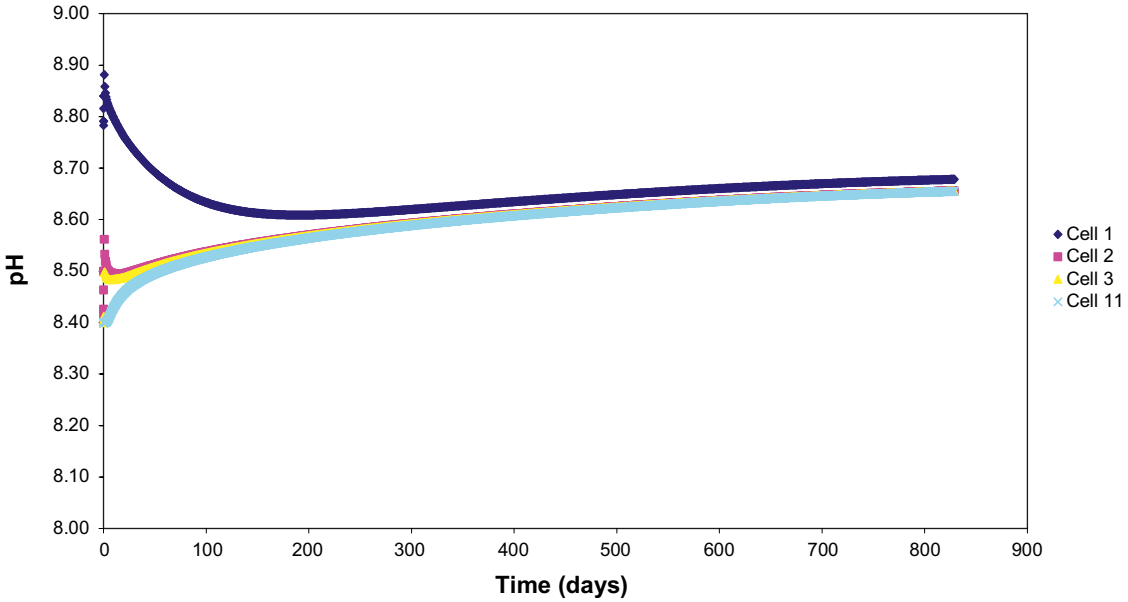

Figure 6-2. *Modelled pH resulting from the corroding iron wire source against time. A diffusion coefficient of 1.2×10^{-10} m^2 s^{-1} was used.*

cells at very early times (up to 1 day) a high pH excursion is predicted due to diffusion from the more alkaline source cell. However, as soon as iron-containing minerals such as magnetite become supersaturated, hydroxyl ions are consumed by the chemical equation:

$$Fe^{2+}_{(aq)} + 2Fe^{3+}_{(aq)} + 8OH^{-}_{(aq)} \rightarrow Fe_3O_{4(s)} + 4H_2O_{(l)} \quad (21)$$

which is shown by the difference between the pH of the source cell and the first bentonite cell at each timestep. However, the pH of the bentonite cells increases slowly to about pH 8.7 due to diffusion from the more alkaline source cell despite buffering by the bentonite surface complexation sites. If there were no formation of magnetite in the bentonite cells, pH values similar to the source cell would be expected within all the bentonite cells after several days.

By the end of the transport simulation, at 829 days, supersaturation of magnetite is predicted and about 21 moles of magnetite is expected to form in the first bentonite cell. This equates to about 63 moles of iron (per litre of porewater and per 80 kg of bentonite) or about 4.4 wt % of iron (Figure 6-3). In addition, a remaining ~ 1.6 moles of sorbed Fe is predicted to be present on the surface complexation sites, within a very small amount of iron existing within the interlayer ion exchange sites (6×10^{-4} moles) and as aqueous species (2×10^{-5} moles). This simulation uses a source cell with a kinetically controlled rate of iron production that had been fitted to the observed rate of gas evolution. The amount of modelled iron available for corrosion per mass of solid has been scaled up from the sample cell, therefore the maximum theoretical amount of iron that could be predicted in the bentonite solid phase is 4.5 wt % (Table 4-1). In comparison, the maximum amount of iron observed in the bentonite solid phase is about 7.5 wt % for the steel wire experiments in compacted bentonite at 30°C, or about 6.6 wt % analysed for the bulk bentonite (Table 4-1 /2/). As a result, a variant case was carried out using a saturated solution of $Fe(OH)_{2(s)}$ as the source cell (see later in this section), which will allow greater amounts of iron present in the solid phase to be predicted.

It is noted that a current limitation of the model means that magnetite will only be supersaturated, and therefore magnetite formation is only predicted, within the first bentonite cell. This model limitation prevents an estimation of the spatial distribution of iron mineral formation, although it is expected that iron mineral formation will be greatest closest to the source of iron, as observed by the electron microprobe analysis.

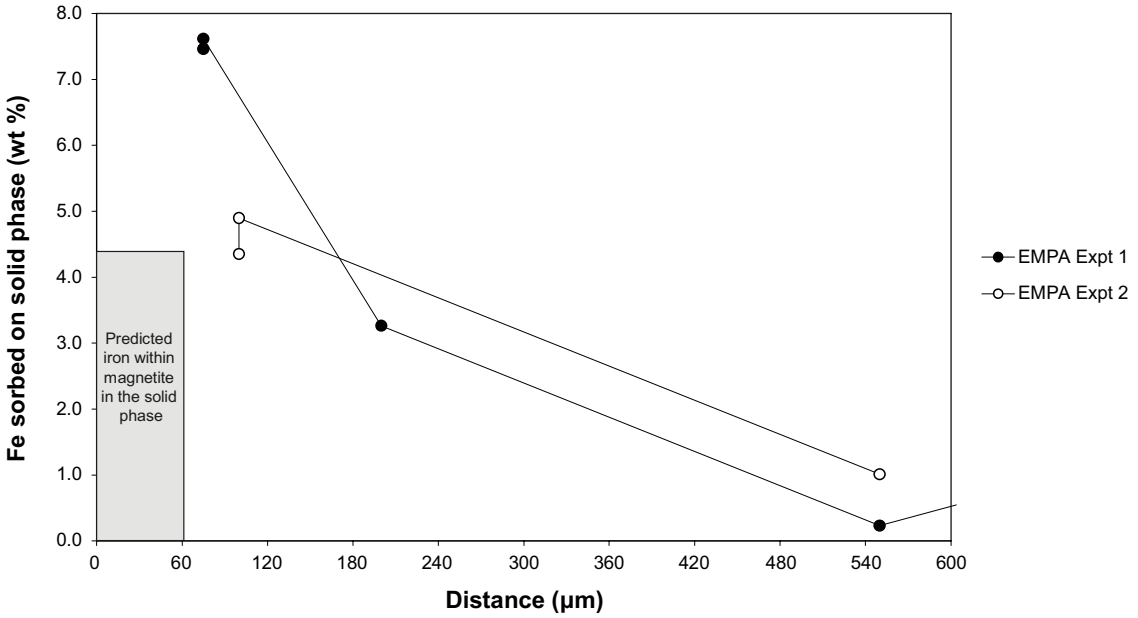

Figure 6-3. *Observed amounts of iron within the bentonite phase (EMPA Expt 1 and EMPA Expt2) and the predicted amount of iron within the first bentonite cell for the base case (blue area).*

The predicted amounts of iron sorbed within the bentonite as a function of distance at the end of the experiments time of 829 days are shown in Figure 6-4. The maximum sorption of iron onto bentonite is calculated to be about 0.16 moles or 0.02 wt % for both surface complexation and ion exchange. It is clear that sorption processes only account for a small proportion of the maximum amount of iron (about 7.5 wt %) observed on the solid phase for the steel wire in compacted bentonite at 30°C. The following paragraphs discuss the predicted iron sorption in more detail.

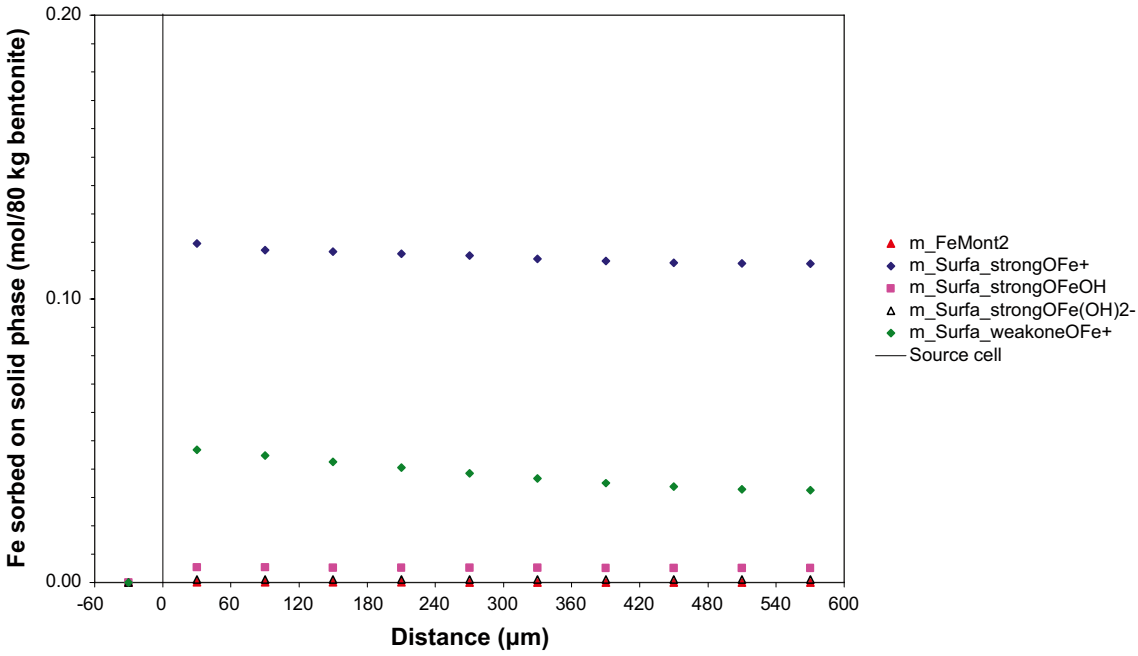

Figure 6-4. *Measured and predicted sorbed amount of iron against distance at 829 days. The sorbed iron represents iron sorbed onto both ion exchange sites and surface complexation sites. A diffusion coefficient of 1.2×10^{-10} m^2 s^{-1} was used.*

The amount of iron sorbed by ion exchange is significantly lower than the amount sorbed by surface complexation because there is much competition for ion exchange sites by the major cations which leads to the lower uptake of iron onto the solid phase. In particular, the aqueous Na concentration is much greater (~ 0.64 mol dm^{-3}) as compared to the aqueous concentration of iron (~ 1×10^{-5} mol dm^{-3}). Therefore, despite the preferential sorption of Fe^{2+} for the solid phase relative to Na^{+}, the Fe^{2+} ions are 'swamped' by the much greater concentration of aqueous Na^{+}. In addition, Ca^{2+} has a higher selectivity coefficient than Fe^{2+} leading to preferential sorption to the solid phase than Fe^{2+}. This contributes to the low sorption of iron onto ion exchange sites.

Surface complexation of iron occurs preferentially onto the strong sites under the model conditions with low concentrations of aqueous iron. However there is a low density of strong sites on the bentonite and the strong sites become fully occupied with iron (hence the near horizontal trend of the blue symbols with distance in Figure 6-4). As a result of full occupation on the strong surface sites, iron sorption also starts to occur on one type of weak surface site (Figure 6-4, green symbols). However, only about 2% of the weak surface sites are predicted to be filled with iron by the end of the experiment.

Variant model case one: thermodynamically controlled rate of iron source term

The first variant case modelled a thermodynamically controlled rate of iron production (a saturated solution of $Fe(OH)_{2(s)}$ in the source cell). A significantly higher aqueous iron concentration was predicted in the source cell (Figure 6-5) than in the kinetically controlled production rate case (the base case, Figure 6-1). As a result, a greater amount of iron containing mineral was predicted to precipitate within the bentonite cells, about 275 moles of magnetite at 829 days. This would give about 58 wt % of iron if all the magnetite precipitated in the first bentonite cell, or about 5.8 wt % of iron if averaged across all ten bentonite cells. This amount of iron within the bentonite phase is significantly more than the observed EMPA value of 7.5 wt % for the iron wire bentonite experiments at 30°C. Therefore this variant case is considered to be one extreme limit, with the base case suggested as a more plausible, lower end limit.

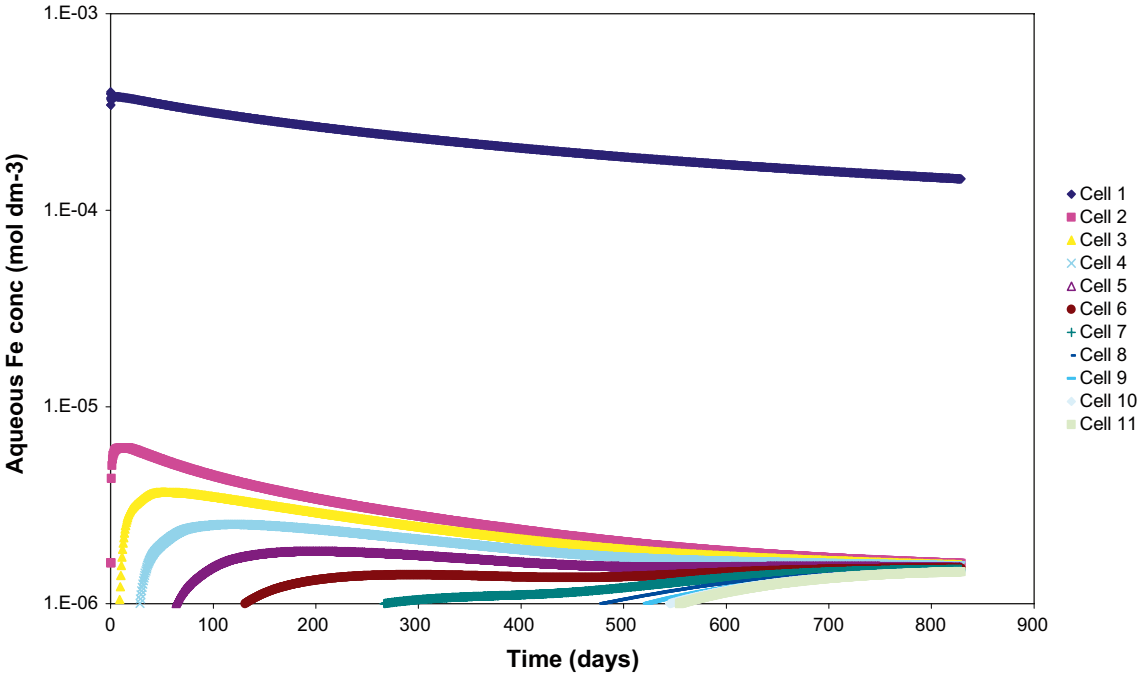

Figure 6-5. *Modelled aqueous Fe^{2+} ions resulting from the corroding iron wire source according to a thermodynamic equilibrium controlled rate of iron production (Cell 1) and in bentonite (Cells 2 to 11) against time. A diffusion coefficient of 1.2×10^{-10} m^2 s^{-1} was used.*

The pH of the source cell in the first variant case was predicted to be about pH 9.1 to 9.2 due to the production of OH^- ions according to the chemical dissolution equation:

$$Fe(OH)_{2(s)} \rightarrow Fe^{2+}_{(aq)} + 2OH^-_{(aq)}. \quad (22)$$

However, the pH of the bentonite cells was maintained at a pH of about 8.6 (after the first few days) because of the precipitation of magnetite that consumes OH^- ions and pH buffering by the surface bentonite sites.

Variant model case two: reduced diffusion coefficent

The second variant case, which used the base case parameters except with a slower diffusion coefficient of 1.2×10^{-11} m^2 s^{-1}, showed similar overall trends to the base case. For instance, the aqueous iron concentration was predicted to have a similar shape, although the long term source cell concentration was higher (1.4×10^{-4} mol dm^{-3}). Likewise, the amount and shapes of the profiles of the iron sorption by ion exchange and surface complexation were similar to the base case and the amount of iron sorbed remained small in comparison to the observations. The amount of magnetite supersaturation within the first bentonite cell was calculated to be similar to the base case, with formation of about 21 moles of magnetite (per litre of porewater and per 80 kg of bentonite) which equates to about 4.5 wt % of iron. When the slower diffusion coefficient was modelled, the long term pH of the source cell is predicted to be about 8.8, which is similar to the base case.

Variant model case three: dilute bentonite porewater

The third variant case used a more dilute bentonite porewater composition to investigate the uptake of iron onto the ion exchange sites. This was important because if all ion exchange sites were filled with sorbed iron then these sites could account for about 2.2 wt % of iron (section 3.3). The base case model showed very low sorption of iron onto ion exchange sites which was assumed to be due to the high ionic strength of the porewater. Therefore a porewater with a lower ionic strength of 0.3 mol dm^{-3} was chosen which corresponded to the literature bentonite porewater model of Bradbury and Baeyens /8/. The porewater composition is reported in column 2 of Table A6 of Appendix 1. The variant simulation results showed that iron uptake onto ion exchange sites is increased by 1.5 times, but still predicts only about 1×10^{-5} wt % of iron, significantly lower than the observations. In all other respects the model predictions are similar to the base case.

6.2 Conclusions of the geochemical transport modelling

Overall, it was shown that ion exchange and surface complexation processes did not provide sufficient sorption to predict the high amount of iron observed in the solid phase. As a result, the supersaturation of iron-containing mineral phases, such as magnetite, was required. The base case model suggested that about 21 moles of magnetite would form in the bentonite, which equates to a maximum of about 4.4 wt % of iron. However, the maximum theoretical amount of iron from the cumulative gas evolution that could be predicted in the solid phase for the base case is 4.5 wt %. In contrast the electron microprobe analysis showed a maximum of about 7.5 wt % of iron within the 30°C compacted bentonite experiments close to the corroding wire source (Figure 1-1), or about 6.6 wt % of iron analysed for the bulk bentonite (Table 4-1). Therefore a variant case with a saturated solution of $Fe(OH)_{2(s)}$ as the source cell was carried out. This predicted that much greater amounts of magnetite could form within the solid phase, with a maximum of 58 wt % of iron. This higher amount is considered to be an extreme scenario, consistent with a higher aqueous concentration of iron in the source cell that is much greater than that predicted by fitting of the measured gas evolution rate data. However, the amount of iron predicted within the solid phase in the base case and this variant case are considered to be bounding scenarios that encompass the experimental results.

Further variant cases with (i) one order of magnitude slower diffusion coefficient predicted a similar amount of magnetite formation to the base case, and (ii) a low salinity porewater solution predicted increased iron sorbed onto ion exchange sites, but this increase hardly affected the overall amount of iron predicted within the solid phase.

This study developed a one-dimensional coupled processes geochemical model of iron transport away from a corroding steel surface into bentonite. The second phase of the experimental programme (not considered within this modelling study) is currently carrying out further corrosion experiments with under a wider set of experimental conditions (groundwater chemistry, pH, temperature and bentonite density. It is considered that further modelling could be useful to investigate this experimental dataset under the different conditions. Similarly, an investigation of these new experiments could scope the uncertainties around the prediction of iron in the solid phase from the total gas evolved and the amounts observed in the solid phase.

7 References

/1/ **Thorsager P, Lindgren E, 2004.** KBS-3H Summary report of work done during Basic Design. SKB R-04-42, Svensk Kärnbränslehantering AB.

/2/ **Smart N R, Carlson L, Hunter F M I, Karnland O, Pritchard A M, Rance A P, Werme L O, 2006.** Interactions Between Iron Corrosion Products And Bentonite, NF-PRO WP2.3 24 month report to SKB.

/3/ **Parkhurst D L, Appelo C A J, 1999.** User's guide to PHREEQC (Version 2) – a computer program for speciation, batch-reaction, one-dimensional transport, and inverse geochemical calculations U.S. Geological Survey Water – Resources Investigations Report 99-4259, 312 p.

/4/ **Bond K A, Heath T G, Tweed C J, 1997.** HATCHES: A Referenced Thermodynamic Database for Chemical Equilibrium Studies, Nirex Report NSS/R379. Database available from http://www.sercoassurance.com/hatches viewed in September 2006.

/5/ **Wanner H, 1986.** Modelling interaction of deep groundwaters with bentonite and radionuclide speciation, Nagra NTB 86-21.

/6/ **Wanner H, Albinsson Y, Karnland O, Wieland E, Wersin P, Charlet L, 1994.** The acid/base chemistry of montmorillonite. Radiochim. Acta 66/67, 157–162.

/7/ **Bradbury M H, Baeyens B, 1997.** A mechanistic description of Ni and Zn sorption on Na-montmorillonite. Part II: modelling. J. Contamin. Hydrol. 27, 223–248.

/8/ **Bradbury M H, Baeyens B, 2002.** Porewater chemistry in compacted re-saturated MX-80 bentonite: Physico-chemical characterisation and geochemical modelling, PSI/NTB 02-10.

/9/ **Bradbury M H, Baeyens B, 2003.** Porewater chemistry in compacted re-saturated MX-80 bentonite, Journal of Contaminant Hydrology 61, 329–338.

/10/ **Ochs M, Lothenbach B, Shibata M, Yui M, 2004.** Thermodynamic modeling and sensitivity analysis of porewater chemistry in compacted bentonite, Physics and Chemistry of the Earth 29, 129–136.

/11/ **Smart N R, 2005.** Written communication by email to F. M. I. Hunter providing bulk and < 2 μm (clay fraction) analysis of MX-80 bentonite used in the experiments, 16th November 2005.

/12/ **Davies C W, 1967.** Electrochemistry, W. Clowes and Sons Ltd.

/13/ **OECD Nuclear Energy Agency, 1997.** Modelling in Aquatic Chemistry, eds. I. Grenthe and I. Puigdomenech.

/14/ **Haworth A, Heath T G, Tweed C J, 1995.** HARPHRQ: A Computer Program for Geochemical Modelling, Nirex Report NSS/R380.

/15/ **OECD Nuclear Energy Agency, 2005.** Chemical Thermodynamics Volume 6 Chemical Thermodynamics of Nickel, eds. F.J. Mompean, M. Illmassène and J. Perrone, Elsevier.

/16/ **Pitzer K S, 1991.** Ion Interaction Approach: Theory and Data Correlation, in "Activity Coefficients in Electrolyte Solutions", 2nd edition, ed. K.S. Pitzer, CRC Press, pp 75–153.

/17/ **Plummer L N, Parkhurst D L, Fleming G W, Dunkle D A, 1988.** A computer program incorporating Pitzer's equations for calculations of geochemical reactions in brines: U.S. Geological Survey Water Resources Investigations Report 88 – 4153, 310 p. Documentation available at http://wwwbrr.cr.usgs.gov/projects/GWC_coupled/phrqpitz/index.html as viewed on 12th October 2006.

/18/ **Kamei G, Oda C, Mitsui S, Shibata M, Shinozaki T, 1999.** Fe(II) – Na ion exchange at interlayers of smectite: adsorption – desorption experiments and a natural analogue, Engineering Geology 54, 15–20.

/19/ **Gaines G I, Thomas H C, 1953.** Adsorption studies on clay minerals: II. A formulation of the thermodynamics of exchange adsorption. J. Chem. Phys., 21, 714–718.

/20/ **Bradbury M H, Baeyens B, 2005.** Modelling the sorption of Mn(II), Co(II), Ni(II), Zn(II), Cd(II), Eu(III), Am(III), Sn(IV), Th(IV), Np(V) and U(VI) on montmorillonite: Linear free energy relationships and estimates of surface binding constants for some selected heavy metals and actinides, Geochimica et Cosmochimica Acta, 69, No. 4, 875–892.

/21/ **CRC Handbook of Chemistry and Physics, 1995.** Eds. D. R Lide and H.P.R Frederikse, 76th edition, CRC Press, Inc, Boca Raton, FL.

/22/ **Lantenois S, Lanson B, Muller F, Bauer A, Jullien M, Plancon A, 2005.** Experimental study of smectite interaction with metal Fe at low temperature : 1. Smectite destabilisation, Clays and Clay Minerals, 53 (6), 597–612.

/23/ **Rodwell W R, 2004.** Summary of a GAMBIT Club Workshop on Gas Migration in Bentonite; Madrid 29–30 October, 2003, Serco Assurance Report SA/ENV-0650.

/24/ **Sellin P, Harrington J, 2006.** Large-Scale Gas Injection Test (Lasgit) – Current Status, presented at International High-Level Radioactive Waste Management Conference 2006, Las Vegas, Nevada, April 30 – May 4 2006.

/25/ **Pruess K, 1987.** TOUGH User's Guide, Nuclear Regulatory Commission Report NUREG/CR-4645 (also Lawrence Berkeley Laboratory Report LBL-20700, Berkeley, CA).

/26/ **Pruess K, 1991.** TOUGH2 – A General Purpose Numerical Simulator for Multiphase Fluid and Heat Flow, Lawrence Berkeley Laboratory Report LBL-29400, Berkeley, CA, 1991.

/27/ **Pruess K, Oldenburg C, Moridis G, 1999.** TOUGH2 User's Guide – Version 2.0, Lawrence Berkeley National Laboratory Report LBNL-43134, Berkeley, CA.

/28/ **Muurinnen A.** Written comm, (1 – (dry density/2.75 g cm^{-3})).

/29/ **Börgesson L, Johannesson L, Sandén T, Hernelind J, 1995.** Modelling of the Physical Behaviour of Water Saturated Clay Barriers: Laboratory Tests, Material Models and Finite Element Application, SKB Report 95–20, Svensk Kärnbränslehantering AB.

/30/ **Horseman S T, Harrington J F, 1997.** Study of Gas Migration in Mx80 Buffer Bentonite, BGS Internal Report WE/97/7 to SKB.

/31/ **de Marsily G, 1986.** Quantitative Hydrogeology, Groundwater Hydrology for Engineers, Academic Press Inc.

/32/ **Luckner L, van Genuchten M Th, Nielsen D, 1989.** A Consistent Set of Parametric Models for the Two-phase Flow of Immiscible Fluids in the Subsurface, Water Resources Research 25, 2187–2193.

/33/ Effects of Post-disposal Gas Generation in a Repository for Spent-fuel, High-level Waste and Long-lived Intermediate Level Waste Sited in Opalinus Clay, Nagra Technical Report NTB 04-06, 2004.

/34/ **Thomas L K, Katz D L, 1968.** Threshold Pressure Phenomena in Porous Media, Society of Petroleum Engineers, 174–184.

/35/ **Bradbury M H, Baeyens B, 1998.** N_2-BET surface area measurements on crushed and intact minerals and rocks: A proposal for estimating sorption transfer factors. Nuclear Technology 122, 250–253.

/36/ **Smart N R, 2007.** Personal communication by telephone to F. M. I. Hunter on 10th Jan 2007.

/37/ **Ochs M, Talerico C, 2004.** Sr-Can: Data and uncertainty assessment, Migration parameters for the bentonite buffer in the KBS-3 concept. SKB TR-04-18, Svensk Kärnbränslehantering AB.

Appendix 1

The underlying chemical thermodynamic porewater model: verification against published literature

Introduction

The porewater composition in compacted bentonite is almost impossible to determine experimentally by chemical analysis; even at very high squeezing pressures it is difficult to obtain large enough quantities of pore water and it is unlikely that this sampled solution is representative of the in situ compacted bentonite porewater. As a result, in general, the properties of compacted bentonite porewater have been evaluated through circumstantial experimental evidence or physical-chemical modelling. Two model approaches have been used in recent evaluations of bentonite porewater chemistry. The traditional approach considers exclusively ion exchange at the siloxane surface (e.g. Wanner 1986 /1/) while more recent models include surface functional OH groups at the clay edge sites in addition to ion exchange (e.g. Wanner 1994 /2/, Bradbury and Baeyens 1997 /3/, 2002 /4/, 2003 /5/). Both electrostatic surface complexation (e.g. /Wanner et al. 1994 /2/, Ochs et al. 2004 /6/) and non electrostatic surface complexation (Bradbury and Baeyens 1997 /3/, 2002 /4/, 2003 /5/) have been implemented within the alternative model approaches.

Verification model input parameters

The approach used in this work has been to take the compacted bentonite porewater equilibrium model developed by Bradbury and Baeyens /4, 5/, and using this as a guide, to set up an equivalent chemical equilibrium model in PHREEQC 12.2. This allows verification of the PHREEQC model against the Bradbury and Baeyens model to check for consistency. Bradbury and Baeyens /4, 5/ based their model on an MX-80 bentonite with similar composition to the MX-80 bentonite used in the experimental study /2/. As a result it was considered appropriate to develop the current MX-80 bentonite model building on the work carried out by Bradbury and Baeyens, after the initial step of verification of the PHREEQC model against their published results.

Bradbury and Baeyens set up a compacted bentonite porewater model in conjunction with measured physical-chemical characterisation data on MX-80 powder. They show that at low water to solid ratios, compacted bentonite acts as a semi-permeable membrane and controls the porewater composition. They take into consideration factors such as the montmorillonite swelling, semi-permeable membrane effects, very low 'free water' volumes[3] and the highly effective buffering characteristics of exchangeable cations and amphoteric clay edge sites. The use of exchangeable cations provides a mechanism to buffer the cation concentrations while the amphoteric clay edge sites fix the pH of the porewater of a re-saturated bentonite. Bradbury and Baeyens used model parameters appropriate for their MX-80 solid; this included:

- MX-80 mineralogy composing:
  - 75% montmorillonite with exchange capacity,
  - calcite, gypsum, celestite, quartz and fluorite minerals in equilibrium with the porewater.

[3] Bradbury and Baeyens discriminate between three types of water in the compacted bentonite as follows /4, 5/. They state that it can be considered that there are three types of water within highly compacted bentonite (dry density > 1,200 kg m^{-3}). When water resaturates under constant volume conditions, most of the water is found within the interlayer space between the alumina and silica layers within the clay platelets (**interlayer water**, probably only one to four monolayers thick). The remaining water can be considered as being associated with the external surfaces of the clay stacks (**double layer water**), or can be considered as interconnected thin films on the outside of the clay stacks when the stack separation is large enough and also as films surrounding the other component minerals grains, such as quartz and feldspar, in the bentonite (**free water**).

- varying bentonite densities,
- liquid to solid ratios of compacted bentonite porewater to MX-80 solid,
- porewater concentrations for chloride concentration from Muurinen et al. 1987 /7/ (cited in /4, 5/),
- appropriate concentrations for aqueous sodium ion (Na^+) to give electrical neutrality.

Other parameters used in the verification modelling exercise and subsequent modelling included:

- Cation exchange and surface complexation parameters (Table A1 to Table A4). Surface complexation with strong sites are included, although these sites are not required for the bentonite porewater modelling (Table A3) but are required for later modelling of iron sorption.
- The initial state of the surface complexation sites as reported by Bradbury and Baeyens 2002 /4/ and the calculated initial state of the surface complexation sites from this work are shown in Table A5.
- The Nagra/PSI Chemical Thermodynamic Data Base 01/01 /8/ was used for all verification exercises.

For the purposes of verification, the PHREEQC model was set up using the above parameters for MX-80 bentonite. The model results were checked against published results (Bradbury and Baeyens 2002 /4/, 2003 /5/) for (i) the prediction of pH in moist bentonite and (ii) the prediction of the aqueous solution composition for two compacted bentonite densities

Table A1. Initial cation loadings on MX-80 bentonite powder in equilibrium in air (after Bradbury and Baeyens 2002 /4/, 2003 /5/).

Cation	Cation occupancies (Eq kg^{-1})
Na	0.668
K	0.013
Mg	0.040
Ca	0.066
Cation exchange capacity	0.787

Table A2. Equilibrium constants for surface complexation reactions (after Bradbury and Baeyens 2002 /4/, 2003 /5/). Note that there are two types of surface complexation site on Na-montmorillonite and that these are denoted by ≡Surfa_weakone and ≡Surfa_weaktwo Each type of weak site has a site capacity of 4.0×10^{-2} mol kg^{-1}.

Surface complexation reaction	log K
$\equiv Surfa\_weakoneOH + H^+ \leftrightarrow \equiv Surfa\_weakoneOH_2^+$	4.5
$\equiv Surfa\_weakoneOH \leftrightarrow \equiv Surfa\_weakoneO^- + H^+$	–7.9
$\equiv Surfa\_weaktwoOH + H^+ \leftrightarrow \equiv Surfa\_weaktwoOH_2^+$	6
$\equiv Surfa\_weaktwoOH \leftrightarrow \equiv Surfa\_weaktwoO^- + H^+$	–10.5

Table A3. Equilibrium constants for protonation/deprotonation surface complexation reactions with strong sites (after Bradbury and Baeyens 1997 /3/). Note that the strong surface complexation sites on Na-montmorillonite are denoted by Surfa_strong≡. Each type of strong site has a site capacity of 2.0×10^{-3} mol kg^{-1}.

Surface complexation reaction	log K
≡Surfa_strongOH + H^+ ↔ ≡Surfa_strongOH_2^+	4.5
≡Surfa_strongOH ↔ ≡Surfa_strongO^- + H^+	–7.9

Table A4. Selectivity constants for ion exchange constants (as reported in Bradbury and Baeyens 2002 /4/, 2003 /5/). Note that the selectivity coefficients are defined according to the convention in Gaines and Thomas 1953 /9/.

Ion exchange reaction	log of selectivity coefficient
Na-montmorillonite + K^+ = K-montmorillonite + Na^+	0.602
2 Na-montmorillonite + Mg^{2+} = Mg-montmorillonite + 2 Na^+	0.342
2 Na-montmorillonite + Ca^{2+} = Ca-montmorillonite + 2 Na^+	0.415

Table A5. Initial state of the amphoteric sites on MX-80 bentonite powder in equilibrium in air at pH 8 and ionic strength of 0.3 mol m^{-3} (after Bradbury and Baeyens 2002 /4/, 2003 /5/). There are two types of surface complexation site on Na-montmorillonite and that these are denoted by ≡Surfa_weakone and ≡Surfa_weaktwo.

Surface site	Fraction of surface complexation sites	Calculated concentration (mol kg^{-1}) Bradbury and Baeyens 2002, 2003	Predicted concentration (mol kg^{-1}) PHREEQC, this work
≡Surfa_weakoneOH	0.56	1.3E–02	1.3E–02
≡Surfa_weakoneOH^+_2	0.44	4.2E–06	4.2E–06
≡Surfa_weakoneO^-	0.00	1.7E–02	1.7E–02
≡Surfa_weaktwoOH	0.99	3.0E–02	3.0E–02
≡Surfa_weaktwoOH^+_2	0.01	9.4E–05*	3.0E–04
≡Surfa_weaktwoO^-	0.00	3.0E–04*	9.4E–05

*Note that it has been assumed that the Bradbury and Baeyens 2002 /4/ values for ≡Surfa_weaktwoOH^+_2 and ≡Surfa_weaktwoO^- have been accidentally switched in their report.

Verification model results: prediction of pH for moist bentonite

The results of the verification of this work against the published results at a range of pH values (and corresponding bentonite densities) are shown in Figure A1. The pink triangles show the published modelling results of Bradbury and Baeyens, while the solid blue triangles show our best fit model verification against their work. Our model used their selection of minerals in equilibrium with the specified aqueous Cl concentration, surface complexation with an initial pre-conditioning of the surface sites to pH 8, ion exchange and an atmospheric partial pressure of CO_2 (i.e. $pCO_2 = 10^{-3.5}$). Bentonite densities corresponding to relevant simulations are marked. The verification of our model against the published data is good at the compacted bentonite densities that are relevant to the experimental programme (i.e. 1,200 to 1,800 kg m^{-3}).

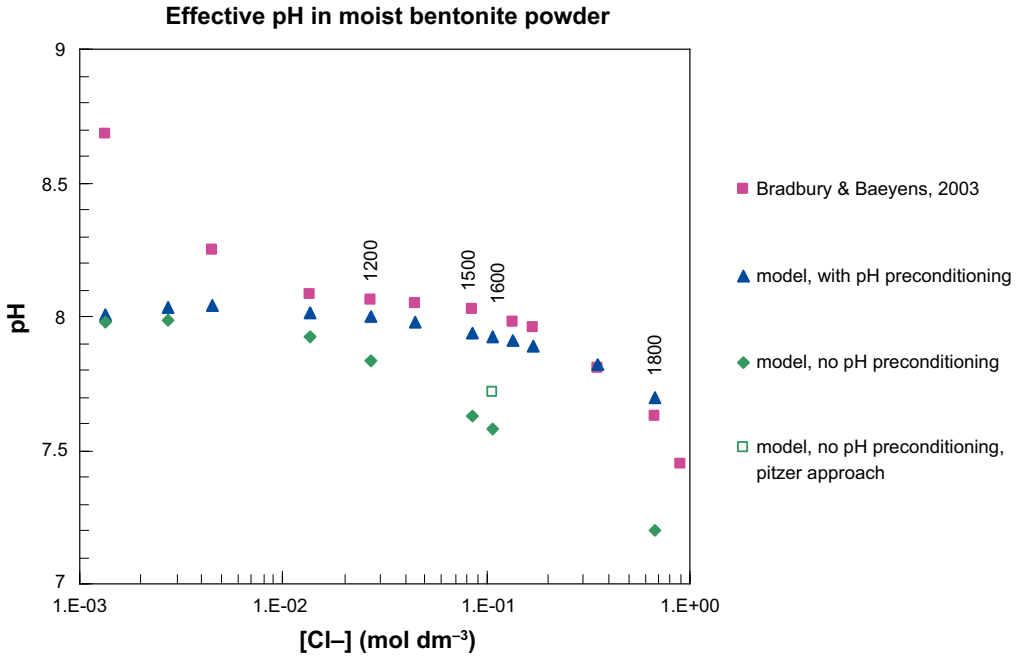

Figure A1. *Effective pH in moist bentonite: verification of our bentonite model against Bradbury and Baeyens 2002 /4/, 2003 /5/. Bentonite densities (kg m^{-3}) corresponding to relevant calculations are marked.*

Variant calculations were carried out without an initial pre-conditioning of the surface sites to pH 8, with an atmospheric partial pressure of $10^{-3.5}$ atm (filled green diamonds), but these calculations did not give such good agreement with the published data. One further calculation without an initial pH preconditioning of the surface sites was carried out using the Pitzer approach to ionic strength (the ionic strength was around 0.6 mol dm^{-3}; open green square) and gave an improved, but still poor, fit against the model data. At high liquid to solid ratios (> 0.1 liquid to solid ratio, corresponding to an aqueous Cl concentration of less than 1.35×10^{-2} mol dm^{-3}) it is clear that there is significant deviation between the two models but the reasoning is not fully understood and may be investigated further.

Verification model results: prediction of aqueous solution composition for moist bentonite

Further verification of our model set up was obtained by matching the aqueous concentrations for two specified MX-80 dry densities of 1,500 kg m^{-3} and 1,600 kg m^{-3}. The results of the verification of the model against the published results for are shown in Table A6. Small differences between the PHREEQC model and the Bradbury and Baeyens model results are noted and are attributed to (i) the use of an independent modelling codes (PHREEQC /10/) rather than MINSORB used by Bradbury and Baeyens which may employ slightly differing approaches, (ii) possible differences in underlying thermodynamic data between the referenced PSI 1991 database and the currently available PSI 2002 database, i.e. it is possible that some relevant data had been updated between the two versions, or (iii) possible differences between approaches for activity correction between the models, although both claim to use the Davies approach of activity correction. However, overall the PHREEQC model gave a good agreement with the results of the Bradbury and Baeyens bentonite porewater model, allowing further work to proceed. As a result, the verified bentonite porewater model was adapted to suit the NF-PRO experimental requirements that use a slightly differing composition of MX-80 bentonite (subsequent sections).

Table A6. Results of model bentonite porewater verification exercise to check PHREEQC model against Bradbury and Baeyens published results 2002 /4/, 2003 /5/. Results are shown for MX-80 dry densities of 1,500 kg m^{-3} and 1,600 kg m^{-3}.

Parameter	Modelled bentonite porewater composition			
	Model reported by Bradbury and Baeyens 2002 /4/, 2003 /5/		Model verification using PHREEQC, this work	
Dry density (kg m^{-3})	1,500	1,600	1,500	1,600
log pCO_2 (bar)	–3.43	–3.48	–3.43	–3.48
pH	8	8	7.99	7.99
Ionic strength (mol dm^{-3})	0.31	0.33	0.34	0.36
C_{inorg} (mol dm^{-3})	8.80E–04	7.79E–04	8.75E–04	7.90E–04
Ca (mol dm^{-3})	9.47E–03	1.01E–02	9.86E–03	1.05E–02
Cl (mol dm^{-3})	6.75E–02	1.08E–01	6.75E–02	1.08E–01
F (mol dm^{-3})	2.19E–04	2.08E–04	2.22E–04	2.13E–04
K (mol dm^{-3})	1.23E–03	1.32E–03	1.38E–03	1.47E–03
Mg (mol dm^{-3})	7.06E–03	7.69E–03	6.79E–03	7.34E–03
Na (mol dm^{-3})	2.43E–01	2.61E–01	2.57E–01	2.73E–01
SO_4^{2-} (mol dm^{-3})	1.04E–01	9.45E–02	1.16E–01	1.08E–01
Si (mol dm^{-3})	1.83E–04	1.83E–04	1.68E–04	1.67E–04
Sr (mol dm^{-3})	8.31E–05	8.87E–05	8.33E–05	8.85E–05

References

/1/ **Wanner H, 1986.** Modelling interaction of deep groundwaters with bentonite and radionuclide speciation, Nagra NTB 86-21.

/2/ **Wanner H, Albinsson Y, Karnland O, Wieland E, Wersin P, Charlet L, 1994.** The acid/base chemistry of montmorillonite. Radiochim. Acta 66/67, 157–162.

/3/ **Bradbury M H, Baeyens B, 1997.** A mechanistic description of Ni and Zn sorption on Na-montmorillonite. Part II: modelling. J. Contamin. Hydrol. 27, 223–248, 1997.

/4/ **Bradbury M H, Baeyens B, 2002.** Porewater chemistry in compacted re-saturated MX-80 bentonite: Physico-chemical characterisation and geochemical modelling, PSI/NTB 02-10, 2002.

/5/ **Bradbury M H, Baeyens B, 2003.** Porewater chemistry in compacted re-saturated MX-80 bentonite, Journal of Contaminant Hydrology 61, 329– 338.

/6/ **Ochs M, Lothenbach B, Shibata M, Yui M, 2004.** Thermodynamic modelling and sensitivity analysis of porewater chemistry in compacted bentonite, Physics and Chemistry of the Earth 29 129–136.

/7/ **Muurinen A, Penttila-Hiltunen P, Rantanen J, Uusheimo K, 1987.** Diffusion of uranium and chloride in compacted Na-bentonite. Report YJT-87-14. Nuclear waste Commission of Finnish Power Companies, Helsinki, Finland.

/8/ **Hummel W, Berner U, Curti E, Pearson F, Thoenen T, 2002.** Nagra/PSI Chemical Thermodynamic Data Base 01/01, Universal Publishers, ISBN: 1-58112-620-4.

/9/ **Gaines G I, Thomas H C, 1953.** Adsorption studies on clay minerals: II. A formulation of the thermodynamics of exchange adsorption. J. Chem. Phys, 21, 714–718.

/10/ **Haworth A, Heath T G, Tweed C J, 1995.** HARPHRQ: A Computer Program for Geochemical Modelling, Nirex Report NSS/R380.

Appendix 2

Example input file for transport calculation

```
TITLE Transport of iron through bentonite clay
# Date: 18th April 2007; User: Fiona Hunter
# Name of case: Transport, IE, SC, Magnetite can ppt, iron kinetic source
# Use nfpro MX-80 composition and sites
# 1L porewater and 80 kg of MX-80 (Compacted bentonite 1600 kg m-3)
# Di(Fe) = 1.2E-10 m2 s-1
# iron kinetic source cell (FionaB exponential rate)
# Phreeqc 2.13 used ; HATCHES nea17 database (no CH4)

SELECTED_OUTPUT
-file Transport_32_final.sel
-pH true
-distance true
-time true
-step true
-totals Fe Fe(2) Fe(3)
-totals Na K Mg Ca Cl C
-totals Surfa_strong Surfa_weakone Surfa_weaktwo Mont
-molalities FeMont2 CaMont2 MgMont2 KMont NaMont Mont-
-molalities         H2 CO3-2 HCO3- H2CO3
-molalities Surfa_strongOFe+ Surfa_strongOFeOH Surfa_strongOFe(OH)2-
-molalities Surfa_weakoneOFe+
-equilibrium_phases CO2(g) Celestite Gypsum MgCO3 cristobalite Calcite
-equilibrium_phases Pyrite Magnetite Fe(OH)2
-kinetic_reactants Fe(s)
-saturation_indices Magnetite Fe(OH)2

EXCHANGE_MASTER_SPECIES
 Mont Mont-
EXCHANGE_SPECIES
#CEC of Montmorillonite from Bradbury & Baeyens, 2003
Mont- = Mont-
 log_k 0.0
Na+ + Mont- = NaMont
 log_k 0.00
K+ + Mont- = KMont
 log_k 0.602
Mg+2 + 2Mont- = MgMont2
 log_k 0.342
Ca+2 + 2Mont- = CaMont2
 log_k 0.415
Fe+2 + 2Mont- = FeMont2
 log_k 0.267 #from Kamei et al., 1999 for I = 0.05 and L/S = 50ml/g
SURFACE_MASTER_SPECIES
          Surfa_strong Surfa_strongOH # Surface a, strong site
          Surfa_weakone Surfa_weakoneOH # Surface a, weak site1
          Surfa_weaktwo Surfa_weaktwoOH # Surface a, weak site2
SURFACE_SPECIES # log_K from Bradbury & Baeyens, 2003
                    Surfa_strongOH = Surfa_strongOH
```

```
        log_k 0.0
                Surfa_weakoneOH = Surfa_weakoneOH
        log_k 0.0
                Surfa_weaktwoOH = Surfa_weaktwoOH
        log_k 0.0

                Surfa_strongOH + H+ = Surfa_strongOH2+ # protonation/deprotonation
        log_k 4.5
        Surfa_strongOH = Surfa_strongO- + H+
        log_k -7.9
        Surfa_weakoneOH + H+ = Surfa_weakoneOH2+
        log_k 4.5
        Surfa_weakoneOH = Surfa_weakoneO- + H+
        log_k -7.9
        Surfa_weaktwoOH + H+ = Surfa_weaktwoOH2+
        log_k 6.0
        Surfa_weaktwoOH = Surfa_weaktwoO- + H+
        log_k -10.5

                Surfa_strongOH + Fe+2 = Surfa_strongOFe+ + H+
        log_k -0.45
                Surfa_strongOH + Fe+2 + H2O = Surfa_strongOFeOH + 2H+
        log_k   -10.44
                Surfa_strongOH + Fe+2 + 2H2O = Surfa_strongOFe(OH)2- + 3H+
        log_k   -19.8
        Surfa_weakoneOH + Fe+2 = Surfa_weakoneOFe+ + H+
        log_k -3.11
PHASES
        Fix_pH
        H+ = H+
        log_k 0.0
        Fix_pE
        e- = e-
        log_k 0.0
        Fe(s)
        Fe(s) + 2H2O = Fe+2 + 2OH- + H2
        log_k -12.03
RATES
Fe(s)
 -start
 10 a = parm(1)
 20 b = parm(2)
 30 c = parm(3)
 40 A0 = parm(4)
 50 rate = (a*exp(-c*(TOTAL_TIME/3600)) + b) * A0 #change rate to seconds; multiply by
surface area; mol m-2 hr-1
 70 moles = rate*(time/3600)          #this is the change in moles of solid over the timestep(shift)
 80 IF(moles > M) then moles = M   #M is the moles at the start of the timestep; if moles is neg
then dissolving solid
 200 SAVE moles
 -end
END

SOLUTION 50
units mol/kgw
water 1.0 #kg
```

```
pH 8.4
EQUILIBRIUM_PHASES 50
Fix_pH -8.4 NaOH 10
SURFACE 50
# Assume 80 kg MX-80 and of this montmorillonite is 87% (69.6kg Mont)
# total moles of sites m2/g surface area g of solid
Surfa_strong     1.39E-01        31.3    69600
Surfa_weakone 2.78E+00        31.3    69600
Surfa_weaktwo 2.78E+00        31.3    69600
-no_edl
SAVE Surface 2-11
END

SOLUTION 1
-units mol/kgw
-temp    25
-water 1.0 #kg
-pH 8.4
-pE -6.76
C        2.46E-03
Ca       9.98E-03
Cl       6.36E-01
K        3.07E-03
Mg       4.94E-03
Na       6.38E-01
KINETICS 1
Fe(s)
-m0              1663.1                  #Number of moles initially
-parms 0.000179147              #parameter a
-parms 1.27061E-05              #parameter b
-parms  0.000664602     #parameter c
-parms  123.84              #surface area (m2)
END

USE surface 2
SOLUTION 2-11 # Equilibrated bentonite porewater
-units mol/kgw
-temp    25
-water 1.0 #kg
-pH 8.4
-pE -6.76
C        2.46E-03
Ca       9.98E-03
Cl       6.36E-01
K        3.07E-03
Mg       4.94E-03
Na       6.38E-01
EQUILIBRIUM_PHASES 2-11
Fix_pE           6.76    O2 1.00E+03
Magnetite        0.0             0.0
Fe(OH)2                  0.0             0.0
# Minerals, SI, moles present in MX-80
#Celestite       0.0             4.36    #SrSO4
#Gypsum                  0.0             4.65    #CaSO4:2H2O
#MgCO3                   0.0             0.00    #Can ppt if supersat.
#Calcite         0.78    7.99    #CaCO3, supersat like in seawater
```

```
#Pyrite          0.0             6.67    #FeS2
#Cristobalite 0.0          39.94   #SiO2
EXCHANGE 2-11
#Total CEC (787 mEq/kg Montmorillonite) from Bradbury & Baeyens, 2003
# 2.04 moles of Montmor per kg of MX-80 (87%); 69.6kg Montmor present
# Name, mol of exchange sites initially
NaMont          53.44
KMont  1.04
MgMont2         1.60
CaMont2         2.64
TRANSPORT 1-11
-cells 11
-shifts 100
-time_step 30
-flow_direction diffusion
-boundary_conditions closed closed
-lengths 11*6.0E-05 #Cell lengths, m: 1 source cells and 10 clay cell
-diffusion_coefficient 1.2E-10 #m s-2
-initial_time 0.0
-print_cells 1-11
-print_frequency 5000
-punch_cells 1-11
-punch_frequency 50
-dump Transport_32_final.dmp #Change this if restart needed!
-dump_frequency 100
#-dump_restart 35800
END
TRANSPORT 1-11
-shifts 100
-time_step 90
-dump Transport_32_final.dmp #Change this if restart needed!
-dump_frequency 100
END
TRANSPORT 1-11
-shifts 71600
-time_step 1000
-dump Transport_32_final.dmp #Change this if restart needed!
-dump_frequency 100
END
```

ISSN 1404-0344
CM Digitaltryck AB, Bromma, 2007